INVESTIGATION INTO KEY INTERFACIAL REACTIONS WITHIN LITHIUM-ION BATTERIES

BY

DANIEL RICHARD VISSERS

DISSERTATION

Submitted in partial fulfillment of the requirements
for the degree of Doctor of Philosophy in Materials Science and Engineering
in the Graduate College of the
University of Illinois at Urbana-Champaign, 2016

Urbana, Illinois

Doctoral Committee:

Professor Paul V. Braun, Chair and Director of Research
Dr. Khalil Amine, Argonne National Laboratory
Professor Andrew A. Gewirth
Associate Professor Shen J. Dillon
Professor Angus Rockett

ABSTRACT

Given the concern of global climate change and the understanding that carbon dioxide emissions are driving this change, much effort has been invested into lowering carbon dioxide emissions. One approach to reduce carbon dioxide emissions is to curtail the carbon dioxide emissions from vehicles through the introduction of hybrid electric vehicles, plug-in hybrid electric vehicles, and electric vehicles. Today, lithium cobalt oxide materials are widely used in consumer electronic applications, yet these materials are cost prohibitive for larger scale vehicle applications. As a result, alternative materials with higher energy densities and lower costs are being investigated. One key alternative to cobalt that has received much attention is manganese. Manganese is of interest for its lower cost and favorable environmental friendliness. The use of manganese has led to numerous cathode materials such as $Li_{1-\delta}Mn_2O_4$ (4V spinel), $Li_{1-\delta}Mn_{1.5}Ni_{0.25}O_4$ (5V spinel), $Li_{1-\delta}(Mn_{1-x-y}Ni_yCo_x)O_2$ (layered), Li_2MnO_3-$Li_{1-\delta}(Mn_{1-x-y}Ni_yCo_x)O_2$ (layered-layered), and Li_2MnO_3-$Li_{1-\delta}(Mn_{1-x-y}Ni_yCo_x)_1O_2$-$Li_{1-\sigma}Mn_2O_4$ (layered-layered-spinel).

The work disclosed in the dissertation focuses on two topics associated with these manganese based cathodes. The first topic is the exceptional cyclic-ability of a high power, high energy density, 5V spinel cathode material ($Li_{1-\delta}Mn_{1.5}Ni_{0.25}O_4$) with a core-shell architecture, and the second is the severe capacity fade associated with manganese dissolution from cathodes at elevated operating temperatures. Both topics are of interest to the Li-ion battery industry. For instance, a 5V spinel cathode represents a viable path to increase both the power and energy density of Li-ion batteries. As its name implies, the 5V spinel operates at 5V that is higher than the conventional 4V lithium ion batteries. Since power and energy are directly proportional to the potential, moving from an operating potential of 4V to 5V represents an increase in both power and energy densities of 25%. When the 5V spinel cathode is coupled with a graphite anode, an energy density of up to 240 Wh kg^{-1} is possible [2]. Secondly, the severe capacity fade associated with the manganese dissolution generally leads to a design with oversized battery packs, like those for the General Motors Chevy Volt, to meet warranty requirements.

The result of this work led to deeper understandings of the underlying mechanisms for the exceptional cyclic-ability of the core-shell 5V spinel and for the severe capacity fade associated with manganese dissolution from the cathode and to a rational approach to resolve the severe capacity fade associated with manganese dissolution.

ACKNOWLEDGEMENTS

First, I would like to thank Professor Paul V. Braun who guided me through the Materials Science and Engineering Ph.D. Program at the University of Illinois Urbana Champaign. His direction and wise counsel enabled me to complete this program.

Second, I would like to thank Dr. Khalil Amine who encouraged me to pursue a Ph.D. and who provided the financial support to enable me to complete this degree. Khalil had my back throughout this endeavor. For this I am truly grateful.

Third, I would like to thank Michael Thackeray whose words, "You only live once", motivated me to take on the Ph.D. even given my numerous laps around the great fire-ball. Michael's Center for Electrochemical Energy Science (CEES), a U.S. Department of Energy funded Energy Frontier Research Center, provided the structure in which I was able to complete the work for my Ph.D. The CEES is a coalition amongst Argonne National Laboratory, the University of Illinois Urbana Champaign, Northwestern University, and Purdue University whose mission is to understand and control the molecular-scale reactivity of electrified oxide interfaces, films and materials that ultimately limits the performance of lithium-ion battery systems. Throughout my Ph.D., I was able to leverage the experience and knowledge of these distinguished institutions.

Fourth, I would like to thank Professor Andy Gewirth, Professor Jeffery Moore, Dr. Zonghai Chen, and Dr. Dennis Dees who all provided the mentoring and wise counsel to enable me to finish this work.

Fifth, I would like to thank my mother, Maryann Vissers, who taught me through her actions the importance of family and family values.

Last, but not least, I'd like to thank my beautiful wife, Allison, my daughter, Eliana, and my son, Jacob, who had to make do with less so that I could finish my Ph.D.

TABLE OF CONTENTS

LIST OF TERMS

A	Active electrochemical surface area
APT	Atom probe tomography
BET	Brunauer, Emmett and Teller Analysis to measure specific surface area
CEI	Cathode-electrolyte interphase
C/n	Rate of charge where n is the time in hours to fully charge or discharge the battery
$C_O(0,t)$	Surface concentration of O at time t O represents the species that is reduced during an electrochemical reaction $(O + ne^- \rightleftharpoons R_{species})$.
$C_R(0,t)$	Surface concentration of $R_{species}$ at time t.
CR2032	Coin cell: 19.9.±0.1 mm diameter and 3.1±0.1 mm height (IEC standard 60086)
CV	Cyclic voltammetry
C45	TIMCAL carbon black (electrically conductive additive for electrodes)
DFT	Density functional theory
E	Potential of the electrode in Volts
EBID	Electron beam-induced deposition
E_F	Fermi level
$\overrightarrow{E_r}$	Radial component of the electric field vector
E^0	Standard electrochemical potential of a reaction in Volts
$f(\alpha)$	Solid phase reaction model
F	Faraday's constant
FCC	Face centered cubic structure
FIB	Focused ion beam
FWHM	Full width at half maximum
g_f	Geometric correction factor for electric field
$\Delta G_b^{\ddagger}$	Activation energy for the oxidation of $R_{species}$
$\Delta G_f^{\ddagger}$	Activation energy for the reduction of O
HAADF	High angle annular dark field
HOMO	Highest occupied molecular orbit
i	Electrical current in Amperes

I_{charge}	Charging current for a cell
IBID	Ion beam-induced deposition
ICP-MS	Inductively coupled plasma mass spectrometry
κ_{el}	Electronic transmission coefficient (related to the probability of electron tunneling)
$k_f(T)$	Forward reaction rate constant
$K_{P,O}$	Ratio of the reactant concentration in the reactive position at the electrode to the concentration at the surface.
$K_{P,R}$	Ratio of the reactant concentration in the reactive position at the electrode to the concentration at the surface.
Li_xC_6	Lithiated graphite (i.e. C_6) where $0 \leq x \leq 1$
$LiMO_2$	Layered lithium transition metal oxide such as $LiCoO_2$
$LiMPO_4$	Olivine lithium transition metal phosphate such as $LiFePO_4$
$Li_xMn_2O_4$	4V spinel cathode $(0 \leq x \leq 1)$
$ln(i)$	Natural log of current, i
LUMO	Lowest unoccupied molecular orbit
M	Concentration of a solute or species in a solution in units of mole/Liter
MCMB	Meso-carbon micro-beads graphite
n	Number of electrons required for the reaction
NMP	N-Methyl-2-pyrrolidone solvent for PVDF
NMR	Nuclear magnetic resonance spectroscopy
O	O represents the species that is reduced during an electrochemical reaction $(O + ne^- \rightleftharpoons R_{species})$.
PVDF	Poly-vinylidene fluoride
ppm	Parts-per-million, 10^{-6}
Q_{charge}	Total charge of cell
R	Universal gas constant
$R_{internal}$	Internal resistance of cell
$R_{product}$	$R_{species}$ represents the species that is produced during an electrochemical reaction $(O + ne^- \rightleftharpoons R_{species})$.
R_t	Radius of a tip
SEI	Solid electrolyte interphase

SEM	Scanning electron microscope
SOC	State of charge
STEM	Scanning transmission electron microscopy
t	Time
T	Absolute temperature in Kelvin
TEM	Transmission electron microscopy
TOF-SIMS	Time-of-flight secondary ion mass spectrometry
UV	Ultraviolet electromagnetic radiation with a wavelength from 400 nm to 10 nm
ν_n	Nuclear frequency factor (s^{-1}) which represents the frequency of attempts on the energy barrier
V	Electrical potential
V_{cell}	Electrical potential of cell
$V_{initial}$	Initial electrical potential of cell
$V_{open-circuit}$	Open circuit electrical potential measured with an electrical current of zero
Wh/kg	Watt-hour-kg^{-1} is a measure of gravimetric energy density
w_O	Work to move the reactant to the reaction location from the average environment
w_R	Work to move the product from the reaction location to the average environment
XPS	X-ray photoelectron spectroscopy
α	Fractional degree of the conversion of the reactants $(0 \leq \alpha \leq 1)$
λ	Reorganization energy
λ_i	Energy associated with the reorganization of the species O.
λ_o	Energy associated with the reorganization of the solvent.

CHAPTER 1

INTRODUCTION TO LITHIUM-ION BATTERIES

To understand the importance of interfacial reactions within lithium-ion batteries, it is important to first understand how a lithium-ion battery operates. The lithium-ion battery is composed of five primary components: the anode, electrolyte, separator, cathode, and current collectors. The anode or negative electrode within lithium-ion batteries is commonly graphite. The electrolyte is a mixture of carbonate solvents and a lithium salt such as $LiPF_6$. The separator is generally a flexible porous polymeric material. The cathode is commonly a lithium transition metal oxide. The current collector for the negative electrode is frequently a thin copper foil and the current collector for the positive electrode is usually aluminum. The operation of a lithium ion battery is analogous to a rocking chair. For instance, when the lithium ion battery is charged, lithium-ions move from the transition metal oxide into the layers of the graphite. In doing so, the oxidation state of numerous transition metal atoms in the cathode increases. Then during discharge, the lithium-ions move from the layers of the graphite and return to the transition metal oxide and the oxidation state of numerous transition metal atoms in the cathode returns to their initial state. The charge and discharge process of the lithium-ion battery is analogous to a rocking chair since the lithium-ion are moving from the cathode to the anode during a charge cycle and from the anode to the cathode during a discharge cycle. Figure 1 illustrates the flow of the lithium-ions and the charge balancing electrons that perform work such as heating a tungsten filament in a light bulb or turning an electric motor in a Tesla Motors Model S.

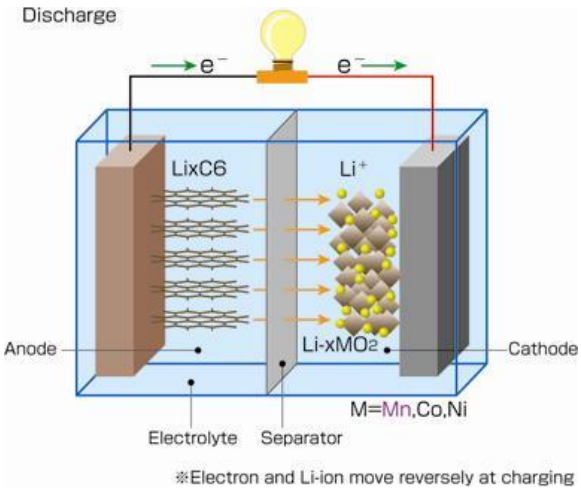

Figure 1 Flow of electrons and lithium ions during the discharge of a lithium ion battery

Now that a high level understanding of the operation of a lithium ion battery has been established, we can move to greater technical depth. Traditional lithium-ion batteries operate at an electrical potential of 4 volts. This potential translates into each electrode having a potential that differs by approximately 4 volts. The electrode potential is generally referenced to a standard reference electrode. For fuel cells, the reference is commonly a hydrogen electrode with an underlying electrochemical half reaction of $2H^+ + 2e^- \rightleftharpoons H_2$. The reference electrode is defined to have an electrical potential of zero volts. A hydrogen reference electrode is a beautiful choice because hydrogen gas bubbling across the electrode surface which keeps the electrode surface clean. In lithium ion battery research, the reference electrode is lithium with an underlying electrochemical half reaction of $Li^+ + e^- \rightleftharpoons Li_s$. Unfortunately, lithium reacts with every organic solvent. Thus, its surface is far from clean. Within lithium-ion battery research, a potential of zero volts corresponds to the lithium half reaction.

Next, it is important to discuss the relationship between the Fermi level of a condensed material, E_F, and the molecular orbits of the electrolyte. The Fermi level is commonly referred to as a hypothetical energy level of an electron. At thermodynamic equilibrium, the Fermi level has a 50% chance of being occupied. The Fermi level of an electrode can be altered by connecting a voltage supply to the electrode and simply changing the voltage of the supply. By increasing the electrical potential of an electrode, the Fermi level of the electrode decreases since electrons are being removed from the electrode material. Next, by decreasing the electrical potential of an electrode, the Fermi level of the electrode increases because electrons are being added to the

electrode material. The altering of the Fermi level of an electrode in the presence of an electrolyte is the heart of electrochemical reactions. Figure 2 illustrates how the Fermi level shifts with various applied electrical potentials.

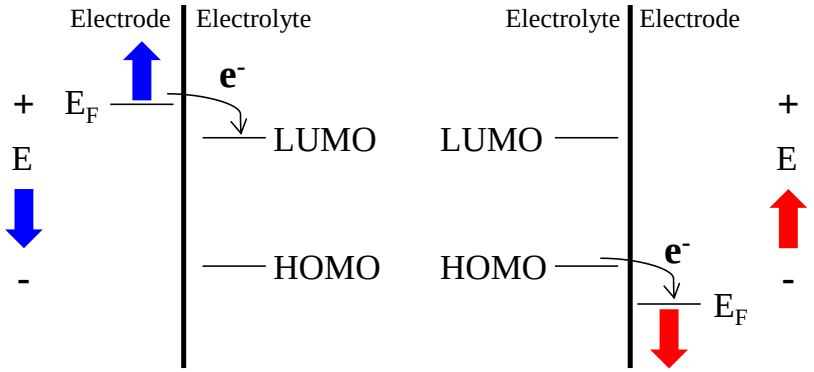

Figure 2 Relationships between the Fermi level, E_F, and the applied electrical potential, E, and between the Fermi level, E_F, and the molecular orbitals.

Figure 2 also illustrates the relative positions of the lowest unoccupied molecular orbit (LUMO) and the highest occupied molecular orbit (HOMO) of commonly used solvents to the Fermi levels of commonly used electrode materials. The electrical potential of the electrodes in Figure 2 align to the relative electrical potentials found in a lithium-ion battery. For instance, the electrode on the left side of the Figure 2 is shown with a lower electrical potential than the electrode on the right side which is similar to the case of a lithium-ion battery where the negative electrode (anode) is on the left side and the positive electrode (cathode) is on the right side as in Figure 1. The left side of Figure 2 shows that the electrolyte can be reduced when the electrical potential of the electrode is sufficiently low as is the case when a graphite electrode is lithiated. The right side of Figure 2 reveals how an electrolyte can be oxidized when the electrical potential of the electrode is sufficiently high as is the case when a 5V spinel electrode is de-lithiated. From this simple figure, we can see how electrolyte decomposition products form at the interface between the electrode and the electrolyte.

These decomposition products at the interface of the negative electrode and the electrolyte in a lithium-ion battery are so important that researchers have given them a specific name, solid electrolyte interphase (SEI). The SEI layer on the graphite is formed during the initial cycling of the lithium-ion battery. Typically, these initial cycles of the lithium-ion battery are referred to as formation cycles and are completed using low charge and discharge currents to allow for a high quality SEI layer to form on the graphite. Once formed, the SEI layer on the graphite allows the

transport of lithium-ions yet inhibits or hinders the further reduction of the carbonate based electrolyte by blocking or reducing the electron transport between the graphite electrode and electrolyte. Thus, the SEI layer plays an important role within the lithium-ion battery.

On the other side of the battery, the decomposition products at the interface of the positive electrode and the electrolyte in a lithium-ion battery have been given a different name, cathode-electrolyte interphase (CEI) layer. This CEI layer forms when the positive electrode (cathode) reaches an electrical potential such that the Fermi level of the electrode is below the potential energy of an electron in the highest occupied molecular orbit of the electrolyte. In this case, the electrolyte is oxidized, or in other words, electrons are removed from the electrolyte.

It should be pointed out that other reactions are known to take place at the electrode-electrolyte interface. For example, a common salt in the electrolyte of lithium-ion batteries is $LiPF_6$. $LiPF_6$ is known to decompose in the presence of water into phosphorous oxy-fluoride (POF_3) and hydrofluoric acid (HF) [3]. The hydrofluoric acid attacks the positive electrodes such as $LiMO_2$ and $LiMPO_4$ [4-6]. For instance, the protons from this acid can reaction with the surface oxygens on the surface of the positive electrode to form water. By this process, surface oxygens can be removed from the positive electrode. Numerous chemical interfacial reactions are possible within the lithium-ion battery.

Since these reactions can generate reaction products at the interface and can even alter the surface layer of the electrode, these reactions can dramatically impact the lithium transport through the interfacial region that in-turn can impact the overall performance of the lithium-ion battery. If the interfacial reaction forms reaction products that contain lithium, then lithium can be removed from the normal operation of the lithium-ion battery. The removal of lithium from the normal operation of the lithium-ion battery induces a capacity fade or a reduction in the overall capacity of the lithium-ion battery which is a major problem if you have to warrantee the useable lifetime of a battery. For these reasons, understanding interfacial reactions within lithium-ion batteries is important.

CHAPTER 2

THEORY OF KINETIC ANALYSIS OF INTERFACIAL REACTIONS

Understanding the theory of kinetic analysis of interfacial reactions establishes a key cornerstone for the work contained in this dissertation because this theory enables us to determine what type of reaction is taking place and how best to slow or stop this reaction. This theoretical foundation also allows us to compare the performance of one electrode surface to another. Understanding interfacial reactions within lithium-ion batteries is important because these reactions dramatically impact the overall performance of the lithium-ion batteries. The interfacial reactions can be categorized into two general classes namely, electrochemical and chemical. An electrochemical reaction is a reaction in which an electron is transferred between a reactant and an electrode. The electron can transfer from the electrode to the reactant so that a reduction of the reactant takes place, or the electron can transfer from the reactant to the electrode so that an oxidation of the reactant takes place. In either case, this reaction is referred to as an electrochemical reaction. Next, a chemical reaction is a reaction that involves one or more reactants which proceeds to one or more products. Chemical reactions can be categorized into numerous classes such as combustion reactions, synthesis reactions, decomposition reactions, single displacement reactions, double displacement reactions, and acid-base reactions. More complex reactions are possible, but for the purposes of this dissertation, we will focus on these two classes of reactions.

Now that a framework for interfacial reactions has been established, we can begin to discuss these reactions and their relevance to lithium-ion batteries. Assume, for the sake of argument, there is a particular lithium-ion battery chemistry that possesses an interfacial reaction that induces a dramatic fade in capacity. Now, let's assume that we have properly analyzed this interfacial reaction and determined that this interfacial reaction is a chemical reaction. What value is this understanding to the scientific community or industry? This understanding is important because it helps to determine how to stop this interfacial reaction and thereby dramatically improve the capacity retention of the lithium-ion battery. For instance, chemical reactions can typically be stopped by keeping the reactants apart. This can be achieved by steric hindrance so one approach to stop a detrimental interfacial chemical reaction is to introduce an inactive material onto the surface where the interfacial reaction is taking place so that the

reactants are unable to come into close proximity of each other. To the scientific community, this work should lead to at least two papers and a potentially valuable patent. To industry, this work should lead to more valuable products and products with lower costs or higher profit margins. Therefore, both the scientific community and industry can benefit from understanding parasitic interfacial reactions. Alternatively, if the interfacial reaction is determined to be an electrochemical reaction, then a potential strategy to slow or stop the reaction would be to introduce an inactive material at the interface that hinders the charge transfer between the reactant and the electrode. Therefore, the proper characterization of the interfacial reaction is valuable in determining how to slow or stop the reaction.

Next, we need to lay a theoretical foundation to model electrochemical and chemical reactions. Thankfully, much theoretical work has been done by others to establish theoretical models for these reactions [7-13]. The kinetic model of an interfacial reaction consists of a kinetic quartet that comprises a reaction model component, nuclear frequency component, electronic tunneling component, and Arrhenius relation component. A kinetic model for a surface reaction between a reactant, O, in a liquid phase and an electrode in a solid phase follows:

$$i = nFAC_O(0,t)k_f(T) \tag{1}$$

where:
i is the electrical current in Amperes.
n is the number of electrons required for the reaction.
F is Faraday's constant.
A is the active electrochemical surface area of the electrode.
$C_O(0,t)$ is the surface concentration of O at time t.
O represents the species that is reduced during an electrochemical reaction $\left(O + ne^- \rightleftharpoons R_{species}\right)$.
0 is the distance from the electrode (i.e the surface is defined as the origin).
t is time.
$k_f(T)$ is the forward reaction rate constant.
T is the absolute temperature.

$\mathrm{AC_O(0,t)}$ is a first-order reaction model where the electrode is a solid phase and its concentration is unity which is a reasonable model when the electrode is gold or platinum. From Marcus' microscopic model, Equation 1 unfolds to:

$$i = nFAC_O(0,t)K_{P,O}\nu_n\kappa_{el}\exp\left(-\Delta G_f^{\ddagger}/RT\right) \tag{2}$$

where:

$K_{P,O}$ is the ratio of the reactant concentration in the reactive position at the electrode to the concentration at the surface.
ν_n is the nuclear frequency factor (s^{-1}) which represents the frequency of attempts on the energy barrier
κ_{el} is the electronic transmission coefficient (related to the probability of electron tunneling).
$\Delta G_f^{\ddagger}$ is the activation energy for the reduction of O.
R is the universal gas constant.

In Equation 2, the frequency (ν_n), electronic tunneling (κ_{el}), and Arrhenius relation $\left(\exp\left(\Delta G_f^{\ddagger}/RT\right)\right)$ components are apparent. The Marcus' microscopic model expands the activation energy for the reduction of O, $\Delta G_f^{\ddagger}$, differently for chemical reactions (3a) and electrochemical reactions (3b) as follows:

$$\Delta G_f^{\ddagger} = \frac{\lambda}{4}\left(1 + \frac{\Delta G^0 - w_O + w_R}{\lambda}\right)^2 \quad (3a)$$

$$\Delta G_f^{\ddagger} = \frac{\lambda}{4}\left(1 + \frac{F\left(E - E^0\right) - w_O + w_R}{\lambda}\right)^2 \quad (3b)$$

$$\lambda = \lambda_i + \lambda_o \quad (4)$$

where:
λ is the reorganization energy.
ΔG^0 is the standard free energy for the chemical reaction.
E is the potential of the electrode in Volts versus a reference electrode.
E^0 is the standard electrochemical potential of a reaction in Volts versus a reference electrode.
w_O is the work to move the reactant to the reaction location from the average environment.
w_R is the work to move the product from the reaction location to the average environment.
λ_i is the energy associated with the reorganization of the species O.
λ_o is the energy associated with the reorganization of the solvent.

Others have used different reaction models to analyze the reaction kinetics for interfacial reactions [12, 13]. In these reaction models, the liquid phase of the reaction is assumed to have a concentration of unity and the solid phase reaction is modelled. The general model follows:

$$i = nF\, {d\alpha}/{dt} = nFf(\alpha)k_f(T) \quad (5)$$

where:
i is the electrical current in Amperes.
n is the number of electrons required for the reaction.

F is Faraday's constant.
α is the fractional degree of the conversion of the reactants $(0 \leq \alpha \leq 1)$.
t is time.
$f(\alpha)$ is the solid phase reaction model.
$k_f(T)$ is the forward reaction rate constant.
T is the absolute temperature.

Again, applying the Marcus' microscopic model for the forward reaction rate constant, Equation 5 becomes:

$$i = nFf(\alpha)\nu_n\kappa_{el}\exp\left(-\Delta G_f^{\ddagger}/RT\right) \quad (6)$$

Now, $f(\alpha)$ can take on many different forms as seen in Table 1 [12, 13].

Table 1: Typical Solid Phase Reaction Models

			$\alpha^m(1-\alpha)^n\left(-ln(1-\alpha)\right)^p$		
	Reaction model	$f(\alpha)$	m	n	P
1	1-D diffusion	α^{-1}	-1	0	0
2		α	1	0	0
3	Power law	$\alpha^{1/2}$	$1/2$	0	0
4	Power law	$\alpha^{2/3}$	$2/3$	0	0
5	Power law	$\alpha^{3/4}$	$3/4$	0	0
6	Zero order	1	0	0	0
7	Contracting cylinder	$(1-\alpha)^{1/2}$	0	$1/2$	0
8	Contracting sphere	$(1-\alpha)^{2/3}$	0	$2/3$	0
9	First order	$(1-\alpha)$	0	1	0
10	Second order	$(1-\alpha)^2$	0	2	0
11	Avrami-Erofeev	$(1-\alpha)\left(-ln(1-\alpha)\right)^{1/2}$	0	1	$1/2$
12	Avrami-Erofeev	$(1-\alpha)\left(-ln(1-\alpha)\right)^{2/3}$	0	1	$2/3$
13	Avrami-Erofeev	$(1-\alpha)\left(-ln(1-\alpha)\right)^{1/2}$	0	1	$3/4$
14	Autocatalytic	$\alpha(1-\alpha)$	1	1	0
15	2-D diffusion	$\left(-ln(1-\alpha)\right)^{-1}$	0	0	-1
16	Diffusion controlled	$\left(1-(1-\alpha)^{1/3}\right)^{-1}(1-\alpha)^{2/3}$			
17	Diffusion controlled	$\left((1-\alpha)^{-1/3}-1\right)^{-1}$			

In any case, each of the kinetic models has pre-exponential components consisting of a reaction model, frequency, electronic tunneling, and other constants, and exponential components consisting of the activation energy and thermal energy terms. For the sake of simplicity, Equation 2 and 3a will be the kinetic model for chemical reactions throughout this dissertation. Likewise, Equation 2 and 3b will be the kinetic model for electrochemical reactions. However, it is important to note that within lithium-ion batteries, the phase of the electrode material is not constant. For instance, a graphite electrode changes phase, Li_xC_6, dramatically through the lithiation process [14]. Each phase of the electrode potentially represents a different

electrochemical or chemical reaction with the reactant. Thus, each component of the kinetic model is dependent upon the phases of the electrode. Although this point is not explicit in Equation 2 since the concentration of the electrode is taken as unity, we cannot forget that the entire equation implicitly assumes a single phase for the electrode. For this reason, there is value in discussing other reaction models for solid reactions such as the ones noted in Table 1.

Now that we have reasonable kinetic models for both electrochemical and chemical reactions, we can begin to design experiments to determine what type of interfacial reaction is taking place in a particular situation. The key difference between the two kinetic models is whether or not the activation energy, $\Delta G_f^{\ddagger}$, is dependent upon the electrode potential, E (refer to Equation 3a and 3b). If there is no measureable difference in the activation energy as the electrode potential is changed while holding the phase of the electrode reasonably constant, then we can conclude that the interfacial reaction is a chemical reaction. If there exists a measurable difference in the activation energy as the electrode potential is changed while holding the phase of the electrode constant, then we can conclude that the interfacial reaction is an electrochemical reaction.

To estimate the activation energy within either kinetic model requires holding the electrode potential constant and changing the temperature and measuring or predicting from a reasonable set of measurements the steady-state current for each temperature. Next, the activation energy can be determined by calculating the slope of the natural log of the steady-state current versus $1/RT$. Equation 7 helps to illustrate this relationship:

$$ln(i) = ln\left(nFAC_O(0,t)K_{P,O}\nu_n\kappa_{el}\right) - \Delta G_f^{\ddagger}/RT \qquad (7)$$

This method can be repeated for different electrode potentials to determine if an interfacial reaction is an electrochemical or a chemical reaction. This method is also useful in comparing the performance of two or more interfacial reactions. For instance, by measuring the activation energies for a 5V spinel electrode reaction with the electrolyte and a core-shell 5V spinel electrode reaction with the electrolyte, one can determine the performance of the outer shell over the inner core 5V spinel relative to the 5V spinel without a shell.

The other valuable piece of information that can be determined from these types of measurements is the combined impact of the pre-exponential factors. In Equation 7, the $ln(i)$-intercept is the natural log of the combined impact of the pre-exponential factors. Although it is

possible to use surface area measurements such as the Brunauer, Emmett and Teller (BET) analysis to estimate and account for the surface area of the electrode, A, in Equation 7, it is more difficult to separate the individual contributions from the frequency (ν_n) and electronic tunneling (κ_{el}) experimentally. Never the less, the combined impact of the pre-exponential factors accounting for the surface area of the electrode is a valuable tool in comparing the performance of two or more interfacial reactions.

The kinetic analysis of a particular interfacial reaction is a valuable tool to characterize the actual reaction, but frequently, it is also important to characterize the surface layer of the electrode using conventional material characterization techniques such as time-of-flight secondary ion mass spectrometry (TOF-SIMS), X-ray photoelectron spectroscopy (XPS) with depth profiling, scanning transmission electron microscopy (STEM), and even atom probe tomography (APT) in some situations. By combining kinetic and materials analyses to investigate a particular interface, a more complete picture of what actually is occurring at the interface is attainable.

CHAPTER 3

EXPERIMENTAL

3.1 Electrochemical analysis

3.1.1 Overall electrochemical performance

To determine the electrical chemical performance of the standard 5V spinel material and the core-shell 5V spinel material, half cells were fabricated using these cathodes and metallic lithium anodes. The standard 5V spinel, Nanomyte^{TM} SP-10, was acquired from NEI Corporation headquartered in Somerset, NJ. The core-shell 5V spinel material was synthesized through a co-precipitation method published earlier [15, 16]. The composition of the standard 5V spinel electrode was: 84 wt% active material, 8 wt% C45, and 8 wt% Kureha 1120 PVDF. The composition of the core-shell 5V spinel follows: 85 wt% active material, 7.5 wt% carbon black, and 7.5 wt% PVDF. The electrolyte for the coin cells was 1.2M $LiPF_6$ in 30 wt% ethylene carbonate and 70 wt% ethyl methyl carbonate from Tomiyama Pure Chemical Industries, LTD. also known as GEN 2 Electrolyte. Celgard 2325 separators were used for coin cells. The CR2032 coin cells were sealed using an automated crimping machine from Hohsen Corporation in the glove box with an argon atmosphere where the oxygen and water content is less than 1 ppm.

Once half cells were fabricated, coin cells were cycled on a MACCOR Series 4000 Automated Test System at room temperature using a voltage window between 3.5V and 4.9V versus $Li^+/Li_{(s)}$. The first three formation cycles applied a charge and discharge rate of C/10 (i.e. ten hours to charge and ten hours to discharge). The next hundred cycles utilized a charge rate of C/3 and a discharge rate of C/2.

To determine the electrochemical performance of the $LiMn_2O_4$ cathode coupled with meso-carbon micro-beads (MCMB) graphite, full cells were fabricated and cycled in varying conditions. In like manner, to assess the electrochemical performance of the $LiMn_2O_4$ cathode and MCMB graphite anode separately, half cells were assembled and cycled at room temperature. The composition of the $Li_xMn_2O_4$ spinel electrode is: 83 wt% TODA 4V spinel, 10 wt% TIMCAL C45, and 7 wt% Solvay PVDF. The composition of the MCMB graphite electrode is: 95.83 wt% Gelon MCMB 615, 4 wt% Kureha 9300 PVDF, and 0.17 wt% oxalic

Content previously published in:
Nano Energy Volume 19, January 2016, Pages 297–306 [1]
ACS Applied Materials & Interfaces (submitted; yet to be published)

acid. The half cells used lithium chips from MTI Corporation as anodes. The electrolyte for the coin cells used the same GEN 2 Electrolyte and Celgard 2325 separators as discussed earlier. The electrodes and separators were dried in a vacuum oven at 75°C overnight to remove any residual water. The CR2032 coin cells were assembled and sealed as noted earlier.

Once the coin cells were fabricated, the coin cells were cycled on a MACCOR Series 4000 Automated Test System at either room temperature or 55°C in an environmental chamber. The coin cells with $LiMn_2O_4$ cathodes coupled with MCMB graphite or lithium anodes were cycled using a voltage window between 3.0V and 4.2V. The coin cells with the MCMB graphite cathode and lithium anode were cycled utilizing a voltage window between 0.001V and 1.5V. The first three formation cycles applied a charge and discharge rate of C/10. The subsequent cycles utilized a charge rate of C/5 and a discharge rate of C/3.

3.1.2 Kinetic analysis

To perform the kinetic analysis of the interfacial reactions, Argonne National Laboratory's (ANL) Electrochemical Reaction Kinetics Analysis System (ERKAS) was applied. This system is composed of two key components. First, to control the operating temperature of the coin cells, an environmental test chamber is used. Two different environment test chambers were used in this work: the Tenney Environmental Test Chamber, Model TJR-A-WF4, from Thermal Product Solutions and the MicroClimate® 1.2 cubic foot benchtop test chamber, Model MCB(H)-1.2, from Cincinnati Sub-Zero. Second, to precisely control and measure the voltage and current of the coin cells, the Keithley 2401 Source Meter is utilized.

To perform the kinetic analysis for the standard 5V spinel and the core-shell 5V spinel, half cells were assembled. The cathodes of these half cells were the standard 5V spinel, core-shell 5V spinel, or carbon black, and the anode is metallic lithium. The carbon black, TIMCAL C45, cathode electrode is used for two reasons. First, it is used to demonstrate that the electrolyte is free from contaminants. Second, since the cathode electrodes typically use C45 as a constituent to improve electrical conductivity, the C45 electrode helps to distinguish between an electrochemical reaction between the C45 and the electrolyte and an electrochemical reaction between the active material and the electrolyte. The kinetic analysis utilized the same standard 5V spinel and core-shell 5V spinel electrodes as discussed earlier in Section 3.1.1. The C45 electrodes were fabricated using a slurry mixture of 50 wt% C45 and 50 wt% Kureha PVDF in

solution of N-Methyl-2-pyrrolidone (NMP). GEN 2 Electrolyte and Celgard 2325 separators were utilized for the coin cells. The CR2032 coin cells were sealed as detailed earlier in Section 3.1.1.

Once the half cells were fabricated, the coin cells completed two and a half formation cycles using a C/10 rate and a voltage window between 3.5V and 4.9V versus $Li^+/Li_{(s)}$ at room temperature and were left in a charged state. The coin cells were then placed into custom fixtures within the Tenney Environmental Test Chamber for the kinetic analysis. For the duration of the analysis, the potential of the coin cell were fixed at 4.9V versus $Li^+/Li_{(s)}$. Kinetic measurements were taken at 5°C, 10°C, 15°C, 20°C, and 25°C. Each temperature was held constant for varying periods of time ranging from 24 hours for the lower temperatures up to five days for the higher temperatures. In doing so, there is sufficient time for the current to reach an equilibrium state.

To investigate the parasitic reactions between the graphite with and without a deposition of manganese and the electrolyte, two different types of half cells were assembled. The first type of half-cell incorporated a formation cycled MCMB graphite electrode acting as the cathode coupled with a metallic lithium anode. The second type of half-cell incorporated a faded MCMB graphite electrode as the cathode coupled with a metallic lithium anode. The formation cycled MCMB graphite cell is a half-cell which has only completed three C/10 formation cycles at room temperature. Hence, this MCMB graphite electrode has no exposure to manganese and represents the baseline. In contrast, the faded MCMB graphite electrode is harvested from a full cell with a $LiMn_2O_4$ cathode and an MCMB graphite anode that completed three C/10 formation cycles at room temperature followed by fifty cycles at 55°C to induce a serve capacity fade. At 55°C, the dissolution of manganese from the cathode electrode is known to occur readily. Thus, the faded MCMB graphite electrode has been extensively exposed to manganese ions within the electrolyte.

Once the half cells were assembled, the coin cells were placed into custom fixtures within the environmental chamber for the high precision electrochemical measurement. The coin cells were warmed to 30°C and subsequently charged to 1.5V and then discharged to 1.2V using a C/10 rate. The potential of the coin cells were then held at following potentials versus $Li^+/Li_{(s)}$: 1.2V, 1.1V, 1.0V, 0.9V, 0.8V, 0.7V, 0.6V, 0.5V, 0.4V, 0.3V, 0.2V, 0.1V, and 0.0V for 15 hours. In doing so, there is sufficient time for the current to reach an equilibrium state. To move between

potentials, a C/10 discharge rate was used. The surface area of the active materials within the MCMB graphite electrode was estimated by multiplying the mass of the active material in the electrode with the surface area per gram value from Gelon's data sheet. The surface area estimates were calculated for each coin cell. Then these estimates were used to normalize the current of each coin cell. The surface areas of the MCMB graphite electrodes ranged from 39.1 cm^2 to 44.0 cm^2.

3.1.3 Cyclic voltammetry (CV)

To understand the electrochemical potentials at which the manganese contaminated SEI reduces the electrolyte, cyclic voltammetry analysis was applied. The cyclic voltammetry analysis used Solartron Analytical 1470E Cell Test System and 1400 Cell Test System, MultiStat Version 1.4b-wd1 software, and a flooded cell. The sweep rate was 0.1 mV/s and the voltage window was 0.1 to -1.7 V versus $Mn^{2+}/Mn_{(s)}$. The flooded cell is composed of a rubber stopper with holes for wires to run through, manganese salt electrolyte, formation cycled MCMB graphite working electrode, manganese reference electrode, manganese counter electrode, and a tall scintillation vial. The manganese salt electrolyte is 30 wt% ethylene carbonate and 70 wt% ethyl methyl carbonate from BASF Corporation with a 29 mmol/L concentration of manganese di-hexafluorophosphate ($Mn(PF_6)_2$).

The $Mn(PF_6)_2$ was synthesized and verified at Argonne National Laboratory using the following procedure. The synthesis of $Mn(PF6)_2$ was carried out in the Argon-filled Schlenk line and an Argon-filled glovebox with oxygen and water level below 1 ppm. $MnCl_2$ (anhydrous), $AgPF_6$ and acetonitrile (CH_3CN) (anhydrous) were purchased from Sigma Aldrich and used as received. A modified procedure for $M(PF_6)_2$ salt synthesis was followed [17].

In an Argon-filled glovebox, 400 mg $MnCl_2$ (3.2 mmol) was suspended in 25 mL CH_3CN, to which was slowly added 25 mL solution of $AgPF_6$ (1.52 g, 6 mmol) in CH_3CN over 10 minutes. The mixture was allowed to stir in dark for more than 12 hours to ensure the completion of the reaction. After completion, colorless solution was collected via filtration through celite. Removal of the CH_3CN solvent under vacuum in a Schlenk line afforded white crystals. Further drying the product in vacuum oven at 75℃ for 10 hours results in analytically pure white powder as the acetonitrile solvated product $Mn(PF6)_2$ (1.5 g). Both the ^{19}F and ^{31}P NMR suggest the high purity of the obtained $Mn(PF_6)_2$ salt. As shown in Figure 3, one set of doublet signal was

observed in ^{19}F NMR spectra at -70.2 ppm (J_{P-F} = 704.5 Hz), corresponding to the clean PF_6^- anions in the solution.

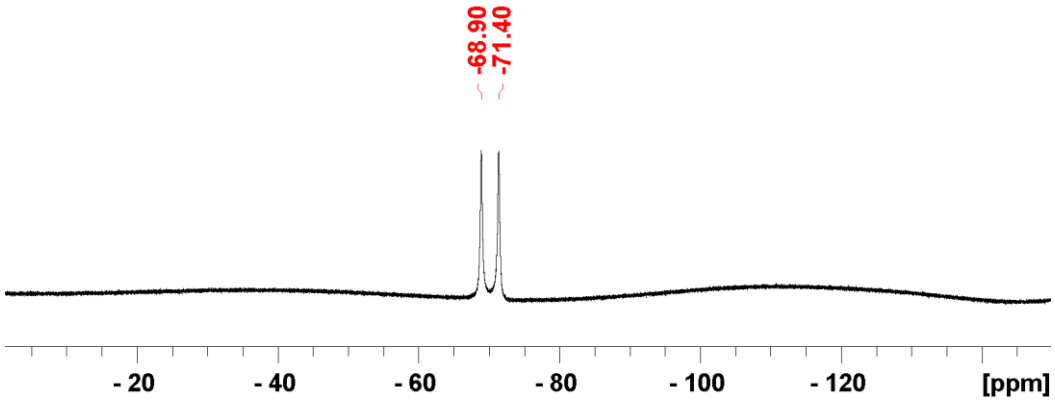

Figure 3 ^{19}F NMR (282.2 MHz) of $Mn(PF_6)_2$ in CH_3CN, J_{P-F} = 704.5 Hz, referenced to BF_3•OE_{t2} (-153 ppm)

Concordantly, one clean set of septet signal was also observed for PF_6^- anions in ^{31}P NMR spectra (Figure 4) with the same P-F coupling constant (J_{P-F} = 704.4 Hz).

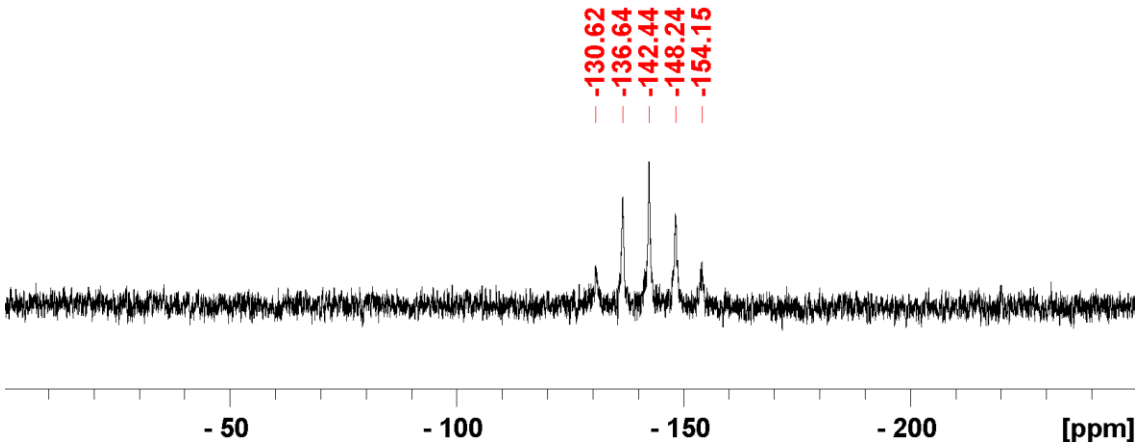

Figure 4 ^{31}P NMR (121.4 MHz) of $Mn(PF_6)_2$ in CH_3CN, J_{P-F} = 704.4 Hz, referenced to H_3PO_4 (0 ppm)

The formation cycled MCMB graphite electrode is the same electrode detailed in Section 3.1.1. The formation MCMB graphite electrode was cycled three times in a flooded half-cell with GEN 2 Electrolyte at a C/10 rate at room temperature. To approximate the surface of the Gelon MCMB within the electrode, the measured loading value for the active material of 2.33 mg/cm^2 was multiplied by the area of the electrode, 0.63 cm^2, to determine the mass of the Gelon MCMB, 1.46 mg. Then, the surface area per gram value of 10^4 cm^2/g from Gelon's product data

sheet was used to calculate the surface area for the Gelon MCMB to be 14.6 cm^2. The manganese metal for the reference and counter electrodes were purchased from Sigma Aldrich Corporation. The flooded cells were assembled and dissembled within a VAC glove box with an argon atmosphere where the oxygen and water content was less than 1 ppm.

3.2 Materials analysis

3.2.1 Atom probe tomography (APT)

The APT technique uses an extremely strong electric field and pulsed UV laser to ionize and desorb atoms from the surface and then a time of flight mass spectrometry for characterization. The APT is useful in determining sub-nanometer structures and concentration gradients. The APT technique requires the specimen to be formed into a sharp nano-scale tip so that a sufficiency large electric field can be achieved. Sharp nano-scale APT specimens from the pristine and long term cycled core-shell 5V spinel electrodes were fabricated utilizing a modified version of the technique published by Thompson [18]. The only notable change to the published technique is a deposition of 50 nm layer of nickel using Northwestern University's ion beam sputter deposition system, a Model IBS/e from South Bay Technologies, to protect the surface of the material from subsequent milling steps. The nickel deposition has trace amounts of aluminum which aid in determining the extent of the protective nickel layer in the latter APT analysis. The other modifications were geometric in nature.

Two focused ion beam (FIB) systems were used in this work, namely, the FEI Helios Nanolab SEM/FIB at Northwestern University, and the FEI Dual Beam 235 FIB at the University of Illinois Urbana Champaign. To protect the samples and milled specimens from long exposures to the atmosphere, a PELCO® SEM Pin Stub Vacuum Desiccator was used.

Scanning electron microscopy (SEM) images of the surface of the un-cycled core-shell 5V spinel electrode are shown in Figure 5. Within this figure, a crystal with a "soccer-ball" like appearance is seen. This crystal structure was selected for APT analysis since it is free from visible voids and defects which lead to a robust specimen which can handle the extreme electrostatic forces established within the APT system on the specimen.

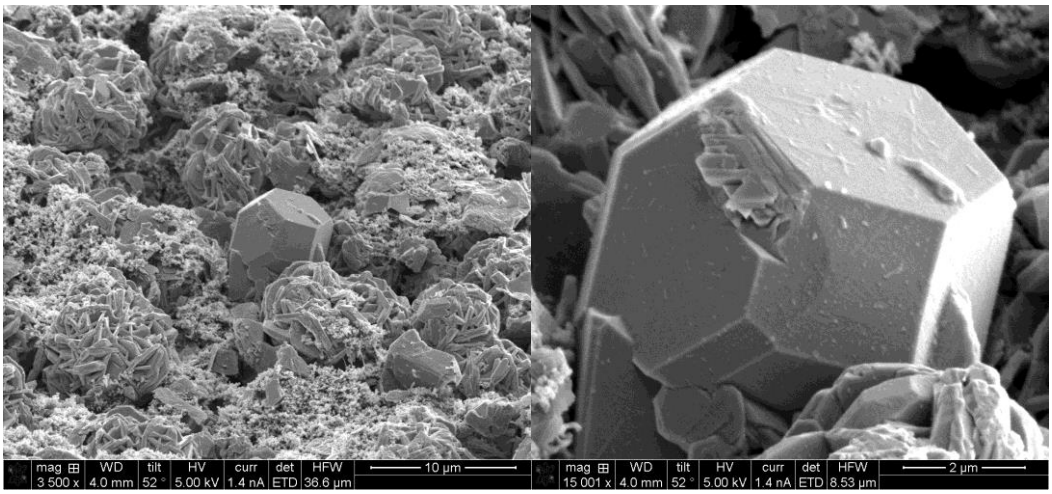

Figure 5 Surface of uncycled core-shell with Ni deposition

Figure 6 represents sequential points within the nano-tip fabrication process on the "soccer-ball" like crystal.

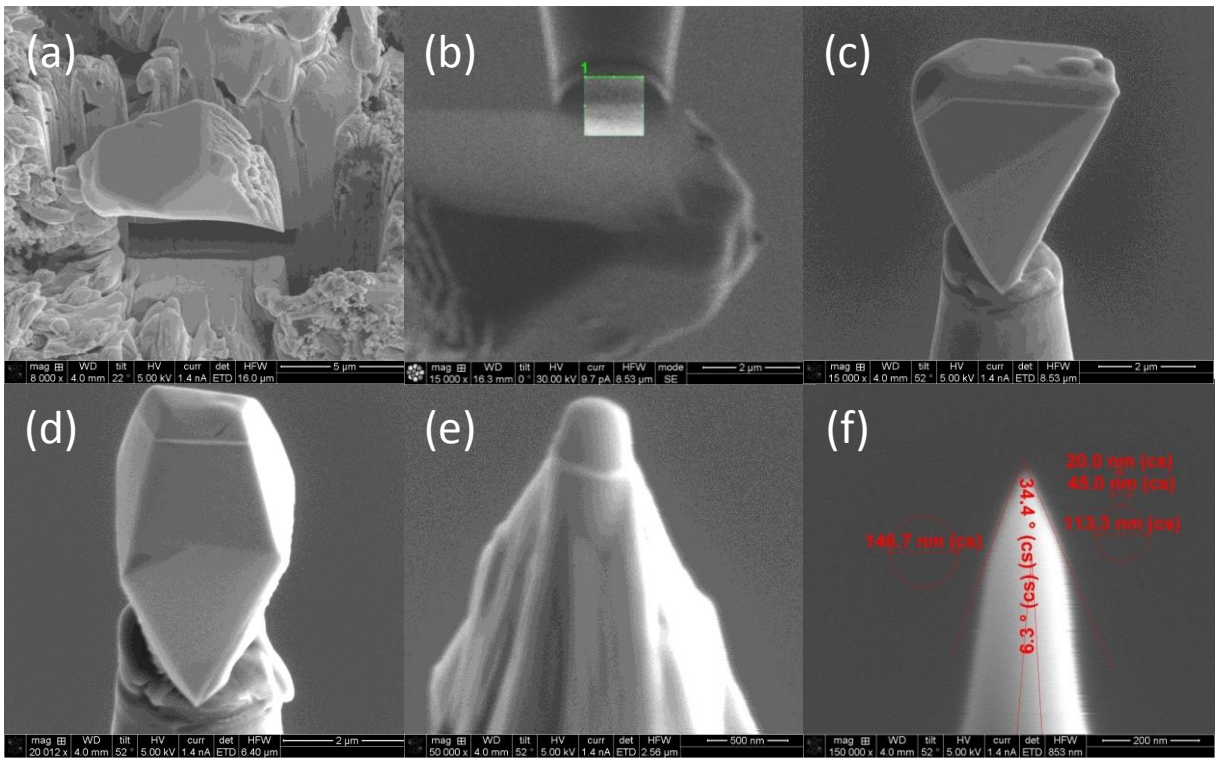

Figure 6 Scanning electron microscopy (SEM) images of the various stages of fabricating a nano-tip to enable the atom probe tomography analysis technique on the core-shell 5V spinel crystal in Figure 1. In (c), (d), and (e), the uppermost layer is platinum, then nickel, then spinel. In (f), the platinum layer is removed leaving a nickel capping layer on the spinel.

A more thorough discussion of the nano-tip specimen preparation is provided in Appendix A.

Similar crystals were used to fabricate nano-tip specimens of the cycled core-shell 5V spinel electrode. The nano-scale specimen tips were analyzed in the CAMECA LEAP 4000 XSi tomograph at the Northwestern University Center for Atom Probe Tomography (NUCAPT) in Evanston, Illinois. The APT data was processed using CAMECA's IVAS™ 3.6.6 data analysis software.

3.2.2 Scanning transmission electron microscopy (STEM)

To perform the STEM analysis on the surface layer of the room temperature cycled core-shell 5V spinel, the samples were sent to the Evans Analytical Group® (EAG) in Raleigh, NC. To protect the surface layer of the sample from subsequent FIB milling steps, EAG first deposited 130 nm of carbon onto the electrode surface using an electron beam-induced deposition (EBID) technique within their FEI Helios dual beam FIB/SEM system. Then using this system, EAG deposited an additional carbon layer onto the electrode surface using an ion beam-induced deposition (IBID) technique. After the carbon deposition, EAG used a proprietary in-situ FIB technique to lift a specimen from the electrode. EAG then mounted the specimen onto a 200 mesh copper TEM grid using IBID of platinum. Afterwards, EAG applied a gallium ion beam to thin a small section of the specimen to an electron transparency thickness. Lastly, EAG utilized their aberration-corrected Hitachi HD2700 scanning transmission electron microscope to acquire the STEM images. The electron beam and the spatial resolution of the aberration-corrected Hitachi HD2700 are approximately 0.14 nm.

3.2.3 Inductively coupled plasma mass spectrometry (ICP-MS)

The ICP-MS analysis was used to measure the concentration of the manganese ions in various electrolyte solutions in varying conditions. The ICP-MS measurements were conducted at Argonne National Laboratory using the following procedure. A portion of each sample was filtered through a syringe mountable filter disk (Whatman PuraDisk TF-25, 0.2 μm pore size) to remove solids. An approximately 2-g portion of each filtered electrolyte solution was transferred to a polypropylene centrifuge tube and weighed. The volatile fraction of the solvent was evaporated by heating in a water bath under a nitrogen stream. Then, the residue was dissolved in 2% nitric acid and brought to a volume of 10 mL. The resulting solutions were analyzed with a Perkin Elmer/Sciex ELAN DRC-II ICP-MS to determine the concentrations of the metals of interest. Concentrations in the electrolytes were calculated from the ICP-MS concentrations, the

mass of sample taken, and the dilution volume. To convert the concentrations in μg/g to equivalent concentrations as μg/mL, the density of the electrolyte solution was applied.

3.2.4 Time-of-flight secondary ion mass spectrometry (TOF-SIMS)

To perform the TOF-SIMS analysis on the surface layer of the faded MCMB electrodes, the samples were sent to the SIMS Service Group of the Evans Analytical Group® (EAG) in Sunnyvale, CA. For the large area analysis (50 μm by 50 μm), the EAG utilized their Cameca IMS 6f with a 3keV O_2 beam. For the small area analysis (5 μm by 5 μm), EAG used their IonTof 5 with a 1keV O_2 beam sputtering and a 30keV Bi beam for analysis. The Bi cycle time for imaging was 30 μs with a 150 ns pulse width. The sputter depths were calibrated using the sputtering rate determined from SiO_2. It should be noted that if the material of the specimen is different from SiO_2, then the TOF-SIMS depth measurement is only an approximate value.

3.2.5 X-ray photoelectron spectroscopy (XPS)

To perform the XPS depth profile analysis on the surface layer of the faded MCMB electrode, the specimens were sent to the Environmental Molecular Sciences Laboratory (EMSL) within the Pacific Northwest National Laboratory (PNNL) in Richland, Washington. The distribution of manganese in the SEI layer on the MCMB graphite was analyzed using XPS. The SEI film was received and mounted for XPS analysis inside an inert gas recirculated glove box operated at <0.2 ppm O_2 and -80°C H_2O dew point. The sample was transferred from the glove box to the XPS spectrometer through the attached XPS sample introduction system in anoxic conditions.

The XPS measurements were performed using a Physical Electronics Quantera Scanning X-ray Microprobe. This system uses a focused monochromatic Al Kα X-ray (1486.7 eV) source for excitation and a spherical section analyzer. The instrument has a 32 element multichannel detection system. A 85 W X-ray beam focused to 100 μm diameter was rastered over a 1.2 mm x 0.1 mm rectangle on the sample. The X-ray beam is incident normal to the sample and the photoelectron detector is at 45° off-normal. High energy resolution spectra were collected using a pass-energy of 69.0 eV with a step size of 0.125 eV. For the Ag $3d_{5/2}$ line, these conditions produced a FWHM of 0.90 eV. The binding energy (BE) scale is calibrated using the Cu $2p_{3/2}$ feature at 932.62 ± 0.05 eV and Au 4f at 83.96 ± 0.05 eV using Ar^+ ion sputter cleaned high purity Au and Cu foils. The depth profiling analysis was performed using 2 kV monoatomic Ar^+ ion source rastered over a 3 mm^2 area of the sample. The sputter rate or depth scale was

determined by referencing to a calibrated sputter rate from a known thickness of SiO_2. It should be pointed out that if the material of the specimen is different from SiO_2, then the XPS depth measurement is only an approximate value. The sample experienced variable degrees of charging. Low energy electrons at 1 eV, 20μA and 7 eV Ar^+ ions were used to minimize this charging.

3.3 Theoretical analysis – density functional theory (DFT)

To calculate if the manganese ions in the GEN2 Electrolyte react with the key constituents of the inner inorganic SEI layer, theoretical density functional theory (DFT) calculations were applied.

For the DFT calculations, energies, forces, and force constants were calculated with the B3LYP hybrid density functional theory [19, 20] with the TZVP basis set [21] as implemented in Gaussian 09 software program [22]. Force constants were used to ensure that structures were minima on the potential energy surface and to estimate the gas phase free energy of each system using standard ideal gas canonical ensemble statistical mechanical expressions. Single point polarized continuum model (PCM) [23] calculations were done at optimized geometries to include solvation effects. A dielectric constant of 55.725 was used to represent an electrolyte composed of 25% ethyl carbonate (EC), 25% ethyl methyl carbonate and 50% propylene carbonate (PC) [24]. Solution phase free energies were calculated by adding the PCM free energies to the gas phase free energies.

CHAPTER 4

CATHODE – 5V SPINEL WITH CORE-SHELL ARCHITECTURE

4.1 Introduction

Lithium-ion batteries utilizing 5V spinel material, $Li_{1-\delta}Mn_{1.5}Ni_{0.5}O_4$, have received considerable interested in recent years for their ability to deliver high energy and power densities. In this chapter, an atomic scale analysis of the surface layer of a core-shell 5V spinel structure where a small amount of the manganese lattice sites have been substituted with cobalt in the shell to reach a stoichiometry of $Li_{1-\delta}Mn_{1.18}Ni_{0.55}Co_{0.27}O_4$ is discussed. The analyses include electrochemical analysis, atom probe tomography (APT) analysis, kinetic analysis of the interfacial reactions, and scanning transmission electron microscopy (STEM) analysis. The APT analysis is performed on the material before and after long-term cycling at room temperature to provide insights into the atomic scale phenomena within the surface layer of the electrode material. Our APT data reveals a 25 to 30 nano-meter (nm) region which forms after cycling. From the analyses, it is believed that the outer few nanometers of this region stabilizes the 5V spinel within the chemical environment of the lithium-ion cell such that its structure is not compromised and thereby enables this material to cycle without significant capacity fading.

Given its higher electric potential and three dimensional lithium ion transport capability, the 5V spinel is an auspicious high energy and high power cathode materials for Li-ion batteries. To date, the main issue with the 5V spinel material is the instability of the interface between the electrolyte and the 5V spinel material [2]. Researchers have developed zinc oxide coatings [25-28] and others researchers have fluorinated electrolytes to address this issue [29-31], yet the issue remains.

In this chapter, a systematic approach is taken to analyze the core-shell 5V spinel material. First, the overall electrochemical performance of the core-shell 5V spinel is compared to the standard 5V spinel using half cells. Next, the composition of the surface layer of the core-shell 5V spinel material is characterized at the atomic scale by APT. Subsequently, to determine the impact of the surface layer within the Li-ion cell, kinetic measurements of the interfacial reactions were acquired using Argonne National Laboratory's (ANL) Electrochemical Reaction Kinetics

Content previously published in:
Nano Energy Volume 19, January 2016, Pages 297–306 [1]

Analysis System (ERKAS). Finally, to assess the structure of the surface layer of the cycled core-shell 5V spinel, scanning transmission electron microscopy (STEM) was applied.

4.2 Overall electrochemical performance

Through cycling half cells of the standard 5V spinel and the core-shell spinel materials, the benefit of introducing cobalt into the outer shell of the 5V spinel is apparent in Figure 7.

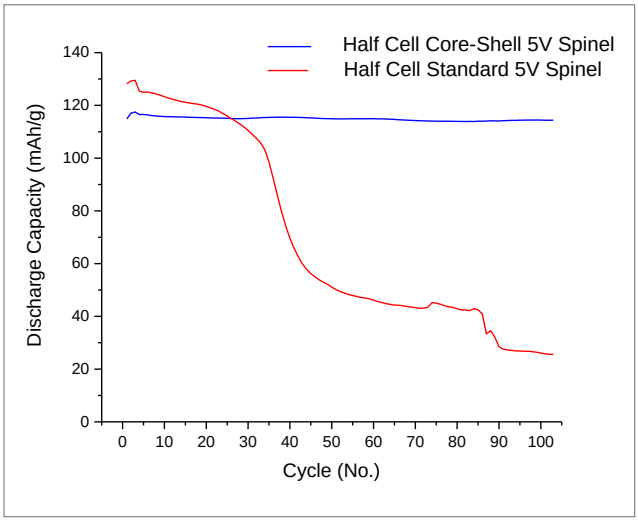

Figure 7 Cycler results for core-shell 5V spinel and standard 5V spinel in half cells

From Figure 7, the substitution of the cobalt into the shell of the 5V spinel dramatically improves the performance of the half cell. To probe further into the half-cell cycler results, the voltage profiles were investigated. The voltage profiles for the first and last cycles of the core-shell 5V spinel and the standard 5V spinel are shown in Figure 8. The first cycles were done with C/10 charge and discharge rates while the hundred and third cycles were done with C/3 charge and C/2 discharge rates.

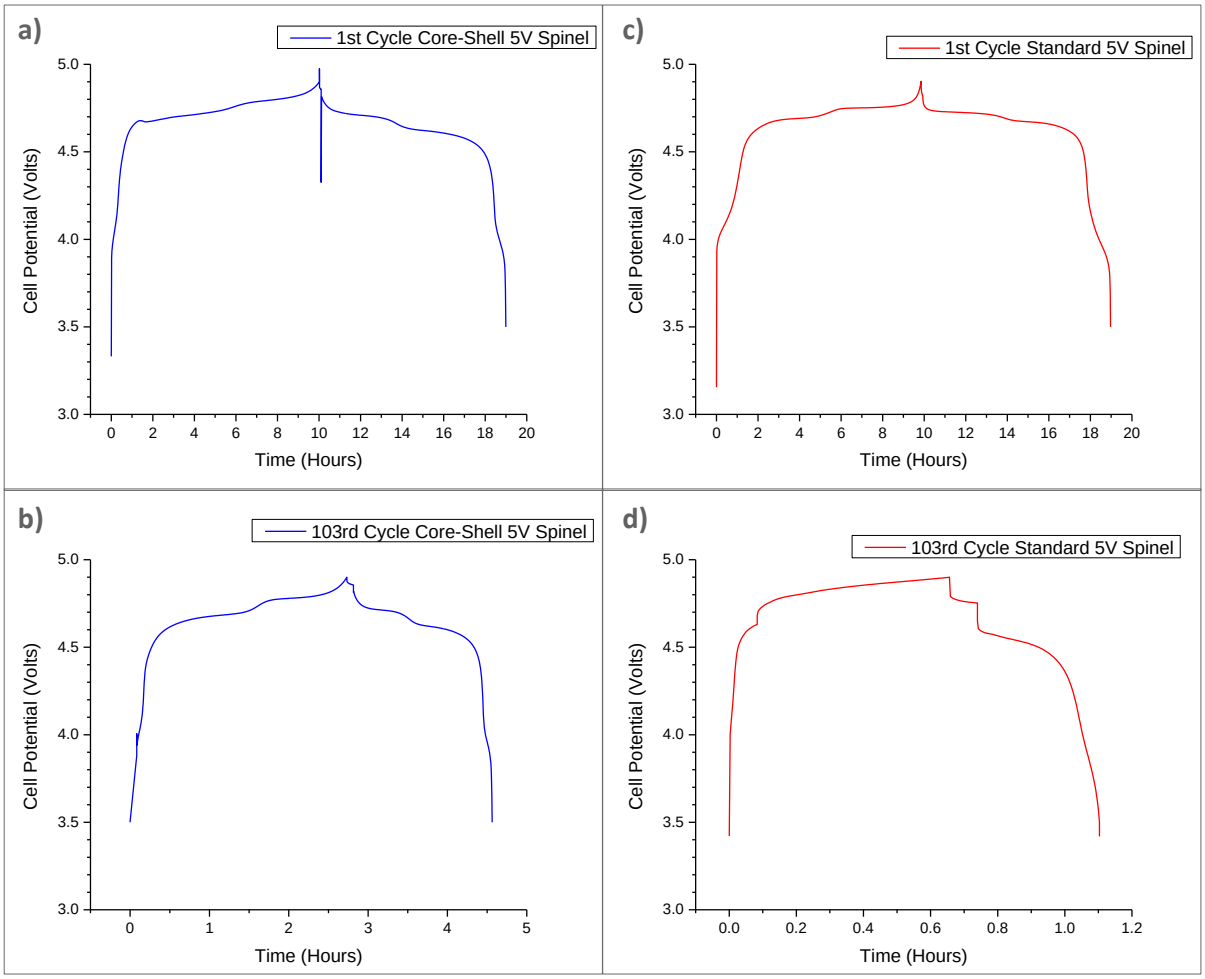

Figure 8 Voltage profiles: a) 1st cycle for the core-shell 5V spinel, b) 103rd cycle for the core-shell 5V spinel, c) 1st cycle for the standard 5V spinel, d) 103rd cycle for the standard 5V spinel in half cells

Figure 8 reveals a couple of key points. First, the core-shell 5V spinel maintains its voltage profile from the first cycle to the hundred and third cycle which implies that the structure of the core-shell 5V spinel remains intact. Second, the voltage profile of the standard 5V spinel changes dramatically from the first cycle to the hundred and third cycle. This voltage profile clearly shows a dramatic increase in the cell impedance and a massive decrease in capacity that are likely related to structural changes especially within the surface layer of the standard 5V spinel.

To begin to understand the mechanism behind the excellent cycle performance of the core-shell 5V spinel, it is important to understand what is occurring at the atomic scale within the surface layer of this material.

4.3 Atom probe tomography results

To understand the atomic scale phenomena within the surface layer of the core-shell 5V spinel, two types of specimens were investigated by the APT technique specifically the un-cycled and cycled material. By comparing the results from the cycled electrode against the uncycled electrode, the changes within the surface layer of the core-shell spinel can be seen. Figure 9 and Figure 10 illustrate the 1D concentration profiles through the surface layer of the un-cycled and cycled core-shell 5V spinel respectively.

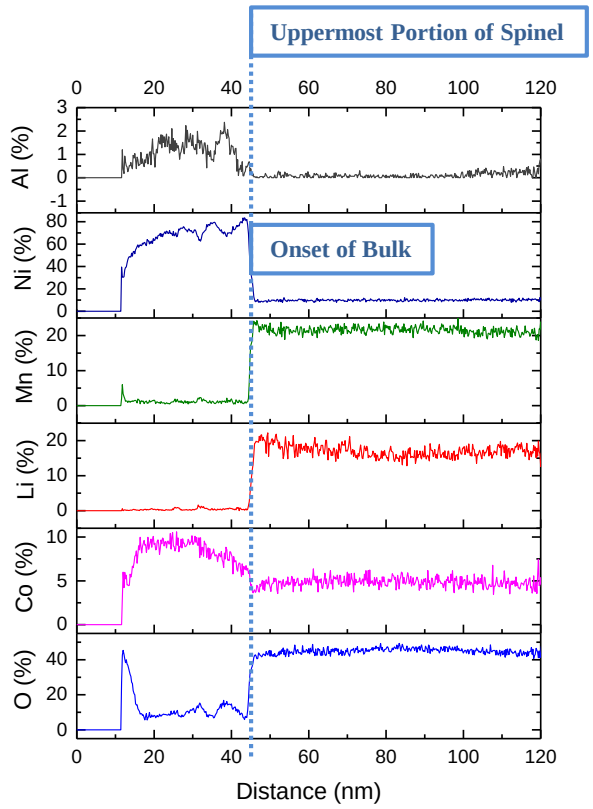

Figure 9 1D concentration profile of uncycled core-shell 5V spinel

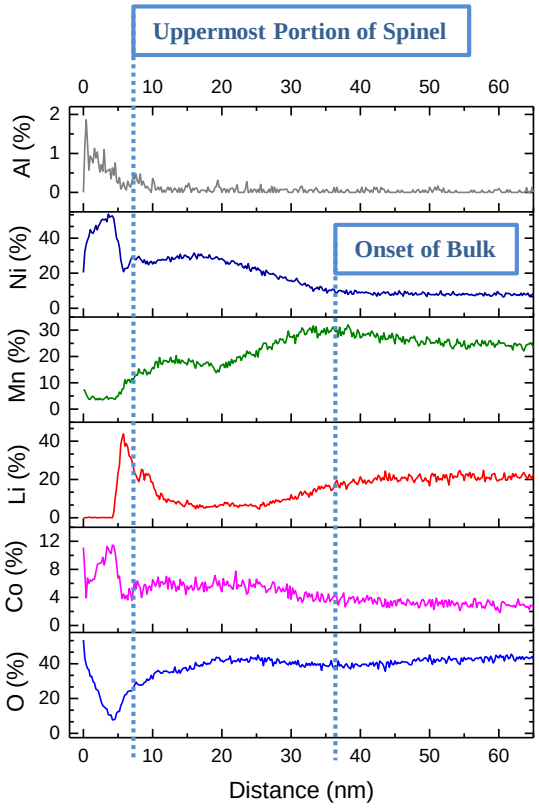

Figure 10 1D concentration profile of cycled core-shell 5V spinel

The leftmost portions of these figures represent the uppermost portion of the nano-tip specimen. The nano-tip specimen starts with a protective nickel deposition and then transitions into the core-shell 5V spinel. The protective nickel deposition is distinguished from the nickel in the spinel by trace amounts of aluminum in the nickel deposition. Therefore, the protective nickel deposition terminates at the same point as does the trace aluminum. This point is also the uppermost portion of the spinel surface. Figure 9 reveals that the surface layer of the uncycled core-shell 5V spinel is identical to the bulk composition which is no surprise since this material

has not been cycled. In stark contrast, Figure 10 reveals a dramatic change within the first 25 to 30 nm of the core-shell 5V spinel surface; afterwards, a bulk concentration is reached.

By further analysis, a more complete atomic-scale picture emerges. In Figure 10, there is an apparent build-up of lithium on the uppermost surface of the spinel which indicates that the lithium-ions are likely tramped within electrolyte reaction products (i.e. CEI) similar to what occurs within solid electrolyte interphase (SEI) on the anode. Following the lithium rich layer, a layer emerges in which the nickel is enriched and the manganese and lithium are depleted. This nickel enriched layer is believed to form as a result of the dissolution of the manganese into the electrolyte (refer to Equation 8 below) and a subsequent diffusion of nickel from the bulk to the surface:

$$2Mn^{3+} \rightarrow Mn^{2+} + Mn^{4+} \qquad (8)$$

In this reaction, the Mn^{2+} dissolves into the electrolyte while the Mn^{4+} remains on the electrode surface. This reaction for the manganese based cathode materials such as the 4V $Li_xMn_2O_4$ is widely referenced in the literature [32-38]. It should be noted that in a 4V spinel, $Li_xMn_2O_4$, half of the manganese is in a 3^+ oxidation state, and the other half is in a 4^+ oxidation state. Therefore, the disproportionation reaction is possible. In contrast, in a pure 5V spinel, $Li_xMn_{1.5}Ni_{0.5}O_4$, an oxidation state of 3^+ is not possible for the manganese since all the manganese is in a 4^+ oxidation state. Therefore, the disproportionation reaction is not possible for the standard 5V spinel assuming that the oxidation state of the manganese on the surface is the same as the bulk which may not be the case [39]. Nickel oxide layers are known to form on the outer most surface of other cathode materials [40]. Thus, the formation of a nickel enriched layer on the core-shell 5V spinel is not peculiar. It should be noted that within the first two nanometers from the surface, the concentration of oxygen is dramatically lower than at a distance of ten nanometers from the surface. Therefore, within the first two nanometers of the core-shell 5V spinel, a very thin layer similar to a nickel (II) oxide material appears to exist. This material is clearly not a pure nickel (II) oxide phase; however, the predominant constituents of this region are clearly nickel and oxygen. One explanation for the dramatic reduction in the concentration of oxygen is that protons within the electrolyte attack the surface oxygen to form water thereby removing oxygen from the surface of the electrode.

Once the nickel (II) enriched layer is formed, it is believed and demonstrated later in the chapter that this layer allows the transport of Li-ions yet hinders the chemical reaction between the electrode surface and the electrolyte. As a result, this layer stabilizes the 5V spinel within the chemical environment of the Li-ion battery.

It should be noted that cobalt is not present in the protective nickel coating yet appears to be present in Figure 9 and Figure 10. This represents an artifact in the way the CAMECA software bins the results. For instance, the nickel isotopes are 58, 60, 61, 62, and 63, and cobalt is 59. Therefore, in the region of the protective nickel coating, the tail from the nickel 58 is creating this cobalt artifact which is evident when the mass spectrum data is inspected more closely. Therefore, it is prudent to always cross check the elemental binning against the mass spectrum which was done for this report.

Additional un-cycled and cycled core-shell 5V spinel specimens were analyzed, and similar results were obtained.

4.4 Kinetic analysis results

To determine if the nickel enriched surface layer of the core-shell 5V spinel impacts the activation energy for the oxidation of $R_{species}$, $\Delta G_b^{\ddagger}$, or the electron tunneling between the constituents of the electrolyte and the cathode material, κ_{el}, a number of electrochemical reaction kinetic measurements were made at varying temperatures. These measurements are based upon Equation 2 and 7 that were discussed in Chapter 2. The only differences are that an oxidation reaction of $R_{species}$ and a backward reaction instead of a forward reaction are occurring. Thus, Equation 2 and 7 become Equation 9 and 10 below:

$$i = nFAC_R(0,t)K_{P,R}\nu_n\kappa_{el}\exp\left(-\Delta G_b^{\ddagger}/RT\right) \quad (9)$$

$$ln(i) = ln\left(nFAC_R(0,t)K_{P,R}\nu_n\kappa_{el}\right) - \Delta G_b^{\ddagger}/RT = ln(i_0) - \Delta G_b^{\ddagger}/RT \quad (10)$$

where:
$C_R(0,t)$ is the surface concentration of $R_{species}$ at time t.
$K_{P,R}$ is the ratio of the reactant concentration in the reactive position at the electrode to the concentration at the surface.
$\Delta G_b^{\ddagger}$ is the activation energy for the oxidation of $R_{species}$.

From Equation 9, it is clear that the steady-state current in our half cells taken at a fixed potential of 4.9V versus $Li^+/Li_{(s)}$ is dependent upon a number of coefficients and variables. The objective

of our work is to determine if any significant difference in either $\Delta G_b^{\ddagger}$ or κ_{el} exists between the core-shell 5V spinel electrode and the standard 5V spinel electrode. Any significant difference in either of these coefficients will provide evidence that the kinetics of the interfacial reactions are different.

To this end, half cells with standard 5V spinel, core-shell 5V spinel, and C45 cathodes, and metallic lithium anodes were fabricated and placed into the ERKAS for evaluation. To ensure that the electrolyte in these cells is free from impurities, half cells with a carbon black, TIMCAL C45, cathode and a metallic lithium anode were used. The operating temperature of the half cells was stepped through the following sequence: 5°C, 10°C, 15°C, 20°C, and 25°C, and the corresponding currents were measured. The results can be found in Figure 11.

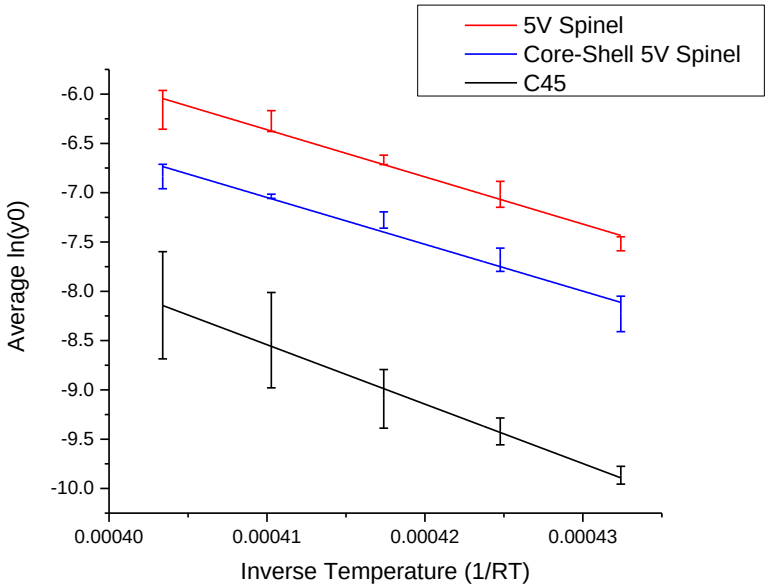

Figure 11 Electrochemical reaction kinetic results: linear fittings for the standard 5V spinel, core-shell 5V spinel, and C45.

Table 2: Fitting results of kinetic study shown in Figure 11

Material	Slope	Slope Error	$ln(i)$-Intercept	$ln(i)$-Intercept Error
Standard 5V Spinel	-47,876.98	4,743.65	13.27	1.98
Core-Shell 5V Spinel	-47,513.96	5,305.28	12.43	2.22
C45	-60,281.51	3,122.67	16.17	1.30

From Figure 11 and Table 2, three points are evident. First, the C45 electrode is much less active than the other two electrodes. Second, since the slopes of the linear fits for the 5V spinel and the

core-shell 5V spinel are comparable, their activation energies, $\Delta G_b^{\ddagger}$, are comparable. As a result, the nickel enriched layer within the surface layer of the core-shell 5V spinel does not impact the activation energy for the oxidation of $R_{species}$.

Next, the ln(i)-intercept points for the standard 5V spinel material and the core-shell 5V spinel material are very close to each other. For instance from Table 2, the ln(i)-intercept point for the standard 5V spinel material is 13.27, and the ln(i)-intercept point for the core-shell 5V spinel material is 12.43. To investigate the ln(i)-intercepts further, it is useful to subtract the ln(i)-intercepts using Equation 10 assuming that the reactant concentration and nuclear frequency terms are comparable for the standard 5V spinel and the core-shell 5V spinel. In doing so, the constants, reactant concentration terms, and nuclear frequency terms drop out, and the following expression remains.

$$ln\left(i_{0,5V}\right) - ln\left(i_{0,CS\ 5V}\right) = ln(A_{5V}) + ln\left(\kappa_{el,5V}\right) - ln(A_{CS\ 5V}) - ln\left(\kappa_{el,CS\ 5V}\right) \quad (11)$$

Brunauer Emmett Teller (BET) Surface Area Analysis revealed that the surface area of the standard 5V spinel, A_{5V}, is 3.61 m^2/g, and that the surface area of the core-shell 5V spinel is 1.069 m^2/g. The mass of the standard 5V spinel on the electrode is 12.9 mg, and the mass of the core-shell 5V spinel on the electrode is 4.75 mg. Given the surface area per gram values, electrodes loadings, and slope intercepts, the difference in the natural log of the electronic transmission coefficients simplifies to the following:

$$ln\left(\kappa_{el,5V}\right) - ln\left(\kappa_{el,Core-Shell\ 5V}\right) = -1.37 \quad (12)$$

$$ln\left(\kappa_{el,5V}/\kappa_{el,Core-Shell\ 5V}\right) = -1.37 \quad (13)$$

By taking the inverse natural log of Equation 13, the relative value of $\kappa_{el,Core-Shell\ 5V}$ to $\kappa_{el,5V}$ is determined:

$$\kappa_{el,Core-Shell\ 5V} = 4 \times \kappa_{el,5V} \quad (14)$$

Therefore, the electronic transmission coefficient, $\kappa_{el,Core-Shell\ 5V}$, that is related to probability of electron tunneling for the core-shell 5V spinel material is a factor of 4 more than the electronic transmission coefficient, $\kappa_{el,5V}$, for the standard 5V spinel material. This result indicates that the nickel enriched layer of the core-shell 5V spinel does not hinder the tunneling of the electrons from the constituents of the electrolyte to the cathode, but promotes the tunneling

of the electrons. The increase in electron tunneling may improve the electrical conductivity among the cathode particles within the electrode which may in turn enable more efficient lithiation and de-lithiation of the cathode which may in turn contribute to its excellent cycle performance.

However, the nickel enriched surface layer of the core-shell 5V spinel does not hinder the oxidation of the electrolyte. Therefore, given the excellent cycle performance of the core-shell 5V spinel and the kinetic analysis results, the performance can only be explained by a reduction of undetermined chemical reaction(s) between the surface of the core-shell 5V spinel and the electrolyte induced by the formation of the nickel enriched surface layer of the core-shell spinel. With the introduction of cobalt into the shell of the core-shell 5V spinel, a nickel enriched surface layer forms during cycling. The nickel enriched surface layer likely forms in three stages. First, the manganese is depleted from the surface layer via the disproportionate reaction (8) at the interface between the electrolyte and the electrode surface. For instance, the Mn^{2+} dissolves into the electrolyte while the Mn^{4+} remains on the surface. Then, nickel and manganese diffuse to the surface from the bulk. Since the manganese continues to dissolve into the electrolyte, over time the surface layer becomes enriched with nickel. However, the key discovery is a dramatic drop in the concentration of the oxygen at the surface seen in Figure 10. The dramatic drop in oxygen occurs over a 2 nm distance from the surface. This drop is likely do to protons within the electrolyte that attack the oxygen at the surface to form water and thereby remove oxygen from the surface. With a closer look at Figure 10, the predominant constituents of the 2 nm surface layer are nickel and oxygen with very similar stoichiometries, and the lesser constituents are lithium, manganese, and cobalt. Thus, this 2 nm "nickel (II) oxide (NiO)" like region at the electrode surface likely enables nickel to stay in an electrochemically inactive oxidation state of 2^+ throughout the cycling process. In the oxidation state of 2^+, the nickel is less chemically reactive with the electrolyte. As a result, the 2 nm "nickel (II) oxide" like surface layer of the core-shell 5V spinel protects the 5V spinel from undetermined detrimental chemical reaction(s) at the interface between the surface of the core-shell 5V spinel and the electrolyte. Thus, the structure of the core-shell 5V spinel remains intact and thereby enables this material to cycle without significant capacity fading.

4.5 Scanning transmission electron microscopy results

To assess the structure of the nickel enriched surface layer of the room temperature cycled core-shell 5V spinel, a high angle annular dark field (HAADF) scanning transmission electron microscopy (STEM) technique was used. Figure 12 represents the HAADF-STEM image of the surface layer of the core-shell 5V spinel. Moving from right to left in the image of Figure 12 is the following sequence: the carbon deposition, the surface layer of electrode, and the bulk of the electrode.

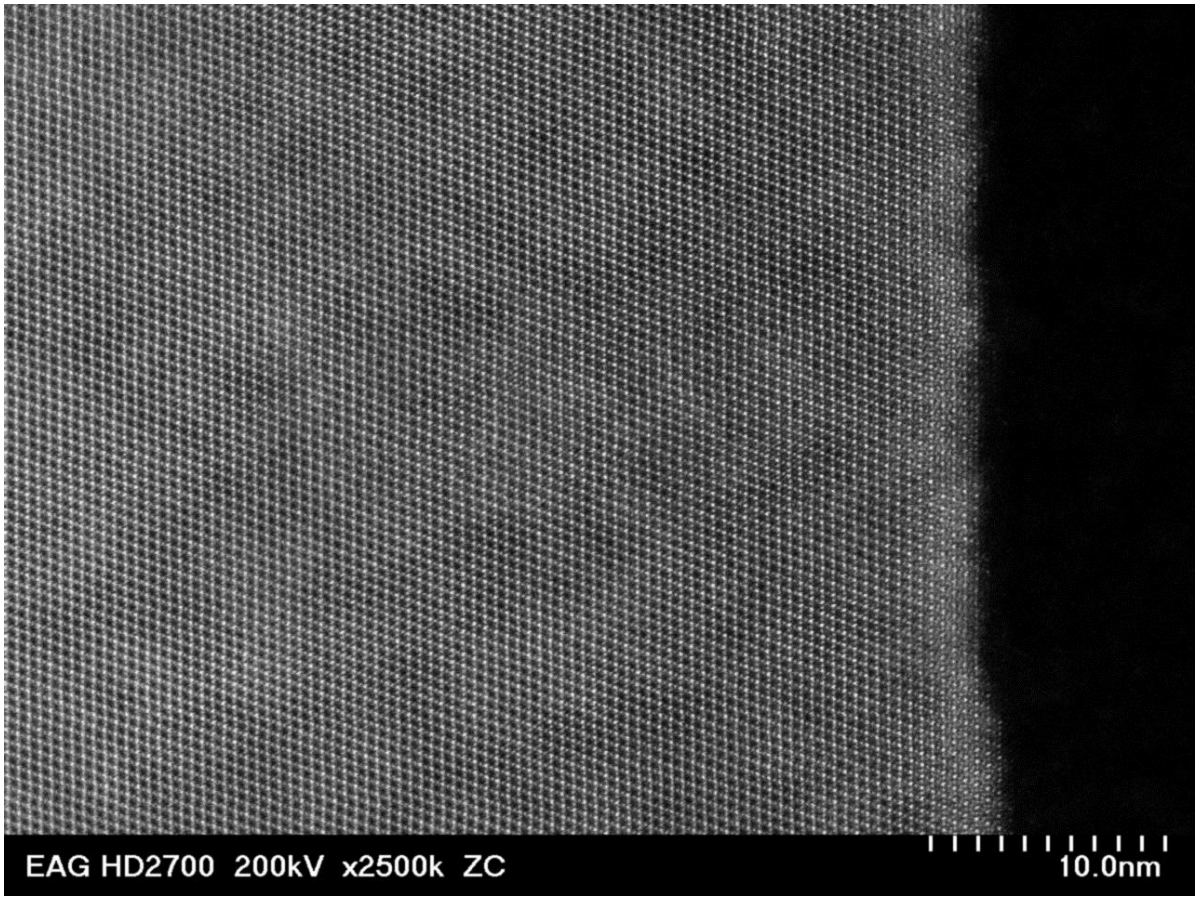

Figure 12 High angle annular dark field scanning transmission electron image of the surface layer of the cycled core-shell 5V spinel

From Figure 12, the periodicity of the higher atomic number elements in the core-shell 5V spinel material remains the same from the bulk to within approximately 1 to 2 nm from the surface. Thus, the structure of a significant portion of the 25 nm to 30 nm nickel enriched surface layer is similar to the structure of the bulk. Hence, for a significant portion of the nickel enriched surface layer, the oxygen face centered cubic structure (FCC) remains intact during the room

temperature cycling of the core-shell 5V spinel which helps to explain the excellent cycle performance of this material. However, for the outermost 1 to 2 nm of the nickel enriched surface layer, the STEM analysis is inconclusive due to imperfections in the surface of the core-shell 5V spinel which demonstrates the inherent value of utilizing APT analysis that is able to account for every other atom.

4.6 Conclusion

To better understand the mechanism for how the substitution of cobalt into the shell of the core-shell 5V spinel structure enables its impressive cycle performance, a systematic approach was used. First, the electrochemical performance of the standard 5V spinel and the core-shell 5V spinel materials were measured in half cells. The half cells demonstrated that the core-shell 5V spinel is able to cycle with minimal capacity loss over a hundred cycles while the standard 5V spinel fades quickly after only thirty cycles. To gain insights into the composition of the surface layer of the core-shell 5V spinel, APT analysis was utilized. This analysis revealed the development of a 25 to 30 nm nickel enriched surface layer where the outermost 1 to 2 nm layer is a "nickel (II) oxide" like phase or nickel (II) enriched layer. Subsequently, through kinetic measurements, it was determined that the nickel enriched surface layer of the core-shell 5V spinel does not alter the activation energy for the oxidation of the electrolyte nor does it reduce the tunneling of electrons from the electrolyte to the cathode. Given the kinetic results and the excellent cycle performance of the core-shell 5V spinel, it was concluded that the 1 to 2 nm "nickel (II) oxide" layer protects the 5V spinel from undetermined detrimental chemical reaction(s) at the interface between the surface of the spinel and the electrolyte and thereby enables its impressive cycle life. It is speculated that the lower concentration of oxygen at the surface enables the nickel at the surface to remain in an electrochemically inactive oxidation state of 2^+ throughout the cycling process and thereby provides chemical stability. Lastly, HAADF-STEM was used and demonstrated that a significant portion of the nickel enriched layer is similar in structure to the spinel bulk which provides evidence that the 1 to 2 nm "nickel (II) oxide" layer protects the spinel structure.

In summary, it has been shown that with the introduction of cobalt into the shell of the core-shell 5V spinel structure, a 1 to 2 nm "nickel (II) oxide" layer forms that protects the 5V spinel from

detrimental chemical reaction(s) at the interface between the electrolyte and the 5V spinel which in turn enables its impressive cycle life.

CHAPTER 5

ANODE – ROLE OF MANGANESE DEPOSITION ON GRAPHITE IN THE CAPACITY FADING OF LITHIUM-ION BATTERIES

5.1 Introduction

Lithium-ion batteries utilizing manganese based cathodes have received considerable interest in recent years for their lower cost and favorable environmental friendliness relative to their cobalt counterparts. However, Li-ion batteries using manganese based cathodes and graphite anodes suffer from severe capacity fading at higher operating temperature. In this chapter, an astute investigation into how the dissolution of manganese impacts the capacity fading within the Li-ion batteries is provided. The investigation reveals that the manganese dissolves from the cathode, transports to the graphite electrode, and deposits onto the outer surface of the inner most solid electrolyte interphase (SEI) layer which is known to be a mixture of inorganic salts (e.g. Li_2CO_3, LiF, and Li_2O) [41-44]. In this location, the manganese facilitates the reduction of the electrolyte and the subsequent formation of lithium containing products on the graphite which removes lithium ions from the normal operation of the cell and thereby induces the severe capacity fade.

The role of manganese dissolution in the capacity fading of lithium-ion batteries utilizing manganese based cathodes and graphite anodes has been studied for roughly three decades which helps to illustrate the complexity of this problem. The dissolution of manganese from the cathode and into the electrolyte is believed to occur through the disproportionation reaction of Mn^{3+} on the surface of $Li_{1-\delta}Mn_2O_4$ to Mn^{2+} and Mn^{4+} (8) discussed earlier in Chapter 4. The Mn^{2+} dissolves into the electrolyte from the cathode surface, and the Mn^{4+} remains on the surface of the cathode. The Mn^{2+} species then migrate and diffuse to the graphite anode and interact with the graphite anode. Komaba, Abraham, and others reported that the dissolution of manganese into the electrolyte induces the formation of additional SEI on the graphite anode which traps the lithium and removes lithium from the normal operation of the lithium-ion battery [45-48]. However, Zhan and others reported that the dissolution of manganese alters the Li-ion transport through the SEI or into the edge plane of the graphite and thereby induces the capacity fade [49-51]. Given these reported experimental results, both phenomena must occur to some degree

Content to be published in:
ACS Applied Materials & Interfaces (submitted; yet to be published)

within the lithium-ion battery, yet a major question remains. The question is which phenomenon dominates the capacity fading: the entrapment of lithium within the electrolyte decomposition products or a dramatic hindrance of the lithium-ion transport through the SEI or into the edge plane of the graphite. To answer this question and to more deeply understand the capacity fading phenomena, electrochemical analysis, density functional theory (DFT) analysis, inductively coupled plasma mass spectrometry (ICP-MS) measurements, parasitic reaction measurements, cyclic voltammetry (CV) analysis, time-of-flight secondary ion mass spectrum (TOF-SIMS) analysis, and x-ray photoelectron spectroscopy (XPS) analysis with depth profiling using Ar^+ ion milling were applied.

5.2 Overall electrochemical performance

To answer the question as to which phenomenon dominates the capacity fading: the entrapment of lithium through the formation of additional SEI or a dramatic hindrance to lithium-ion transport through the SEI, a set of experiments were run in which full cells were subject to the subsequent steps: three formation cycles at room temperature, fifty cycles in accelerated capacity fading conditions (i.e. 55°C), and three cycles at C/10, C/20, and C/30 rates at room temperature. Varying the C-rate is crucial in determining the root cause of the capacity fade. For instance, if the capacity fade is dependent upon a dramatic increase in internal resistance of the cell, then the capacity of the cell can be restored by charging and discharging the cell very slowly. Mathematically, Equation 15 illustrates the relationship between the capacity of the cell and the internal resistance of the cell:

$$Q_{charge} = \int_{V_{initial}}^{V_{cell}=V_{open\ circuit}+R_{internal}I_{charge}} I_{charge}dt \tag{15}$$

If the charging current, I_{charge}, and the internal resistance, $R_{internal}$, are qualitatively small in Equation 2, then V_{cell} is approximately equal to $V_{open\ circuit}$. These conditions are met when a C/10 charging rate is used during the first charging cycle. Since a C/10 charging current requires ten hours to fully charge a cell, this current is qualitatively small. During the first charging cycle, the cell internal resistance is typically at a minimum since the SEI has yet to be adversely affected. As a result, the product of I_{charge} and $R_{internal}$ (i.e., the potential drop across the internal resistance) is qualitatively small. Thus, by using Equation 2 and the initial charging cycle with a C/10 rate, we were able to correlate the cell voltage, V_{cell}, directly to the state of

charge (SoC). Figure 3 and Table 1 show the SoC for the first charging cycle of a coin cell with a $LiMn_2O_4$ cathode and an MCMB graphite anode.

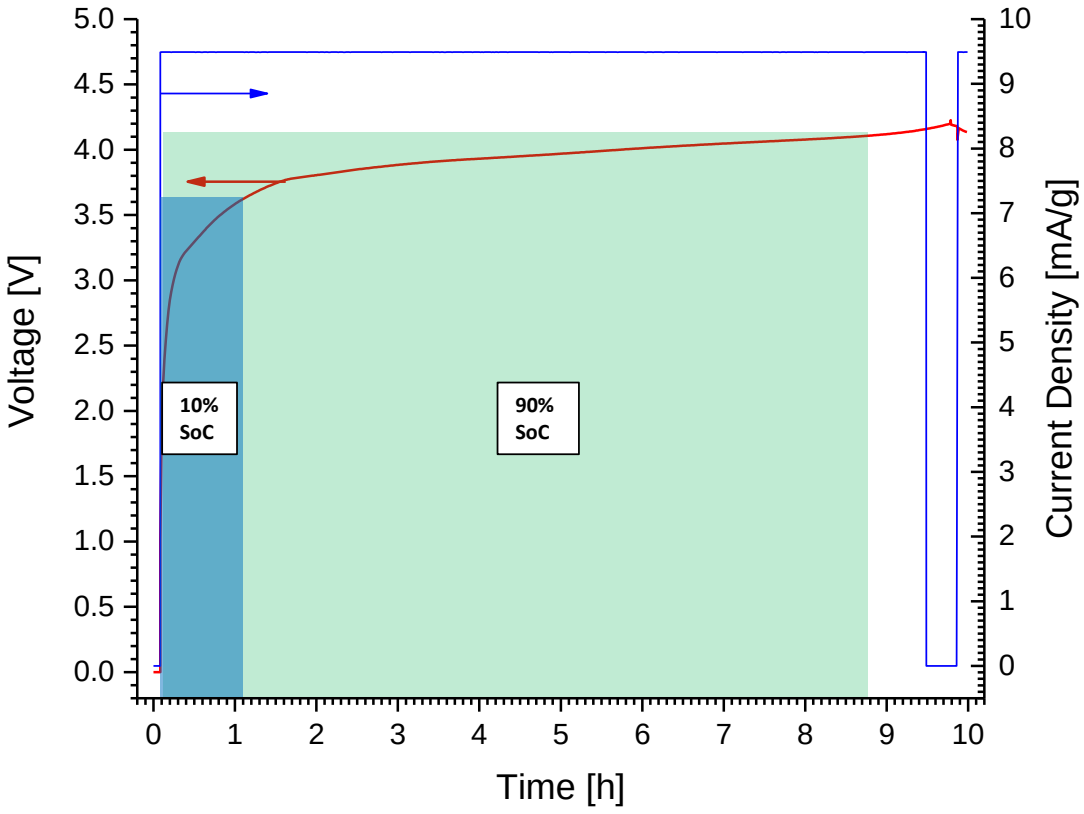

Figure 13 Voltage profile for $LiMn_2O_4$ cathode against MCMB graphite anode using C/10 rate

Table 3: Measured state of charge

State of Charge [%]	Voltage [V]
10	3.61
20	3.81
30	3.88
40	3.93
50	3.97
60	4.01
70	4.04
80	4.07
90	4.11
100	4.20

From Figure 13 and Table 3, a capacity fade of 90% from purely an internal resistance using a C/5 charging rate and a constant voltage window between 3V and 4.2V correlates to the $V_{open-circuit}$ only reaching 3.61V. Hence from Equation 15, $R_{internal}$ is $0.59/I_{C/5}$. Now, using this term for $R_{internal}$, a C/30 charging rate, and V_{cell} of 4.2V in Equation 15, the $V_{open-circuit}$ is

4.1V that is equivalent to a 90% state of charge. In other words, if the capacity fade of the battery is primarily due to a dramatic increase in the internal resistance and the capacity fade is 90% with a C/5 charging rate, then the capacity will be virtually restored by using C/30 charging rate. Appendix B provides a further explanation of the relationship between the internal resistance of a battery and the associated capacity fade using Ohm's law and Kirchhoff's circuit laws.

Equipped with this understanding, we embarked on a set of experiments in which full cells were subject to severe fading conditions followed by cycling at C/10, C/20, and C/30 rates. Figure 14 shows the results of these experiments.

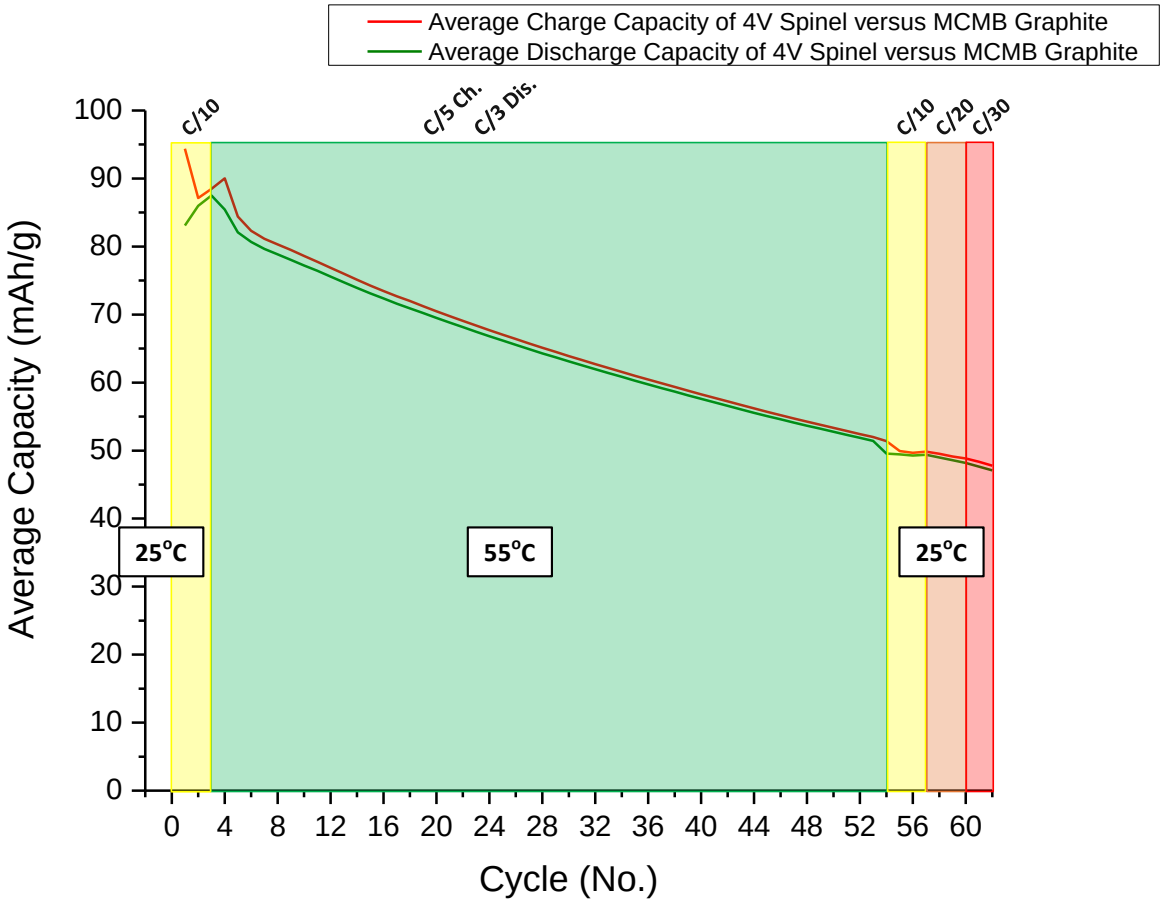

Figure 14 Average capacity for cell with $LiMn_2O_4$ cathode and MCMB graphite anode

From Figure 14, the capacity fade from the first cycle to the fifty-third cycle is roughly 45% which is much less than 90%. Thus, given our previous argument, the capacity of the cell should virtually recover to its initial value with a C/30 rate, but it clearly does not recover. Therefore, the dominate contributor to the capacity fade of a cell with a $Li_{1-\delta}Mn_2O_4$ cathode and an MCMB graphite anode is not a dramatic increase in the internal resistance of the cell.

To demonstrate this point further, the electrodes from the faded coin cells were harvested and placed into half cells. These half cells were then cycled at room temperature. In doing so, deeper insights into the capacity fading of these cells were achieved. Figure 15 illustrates the results from these half cells.

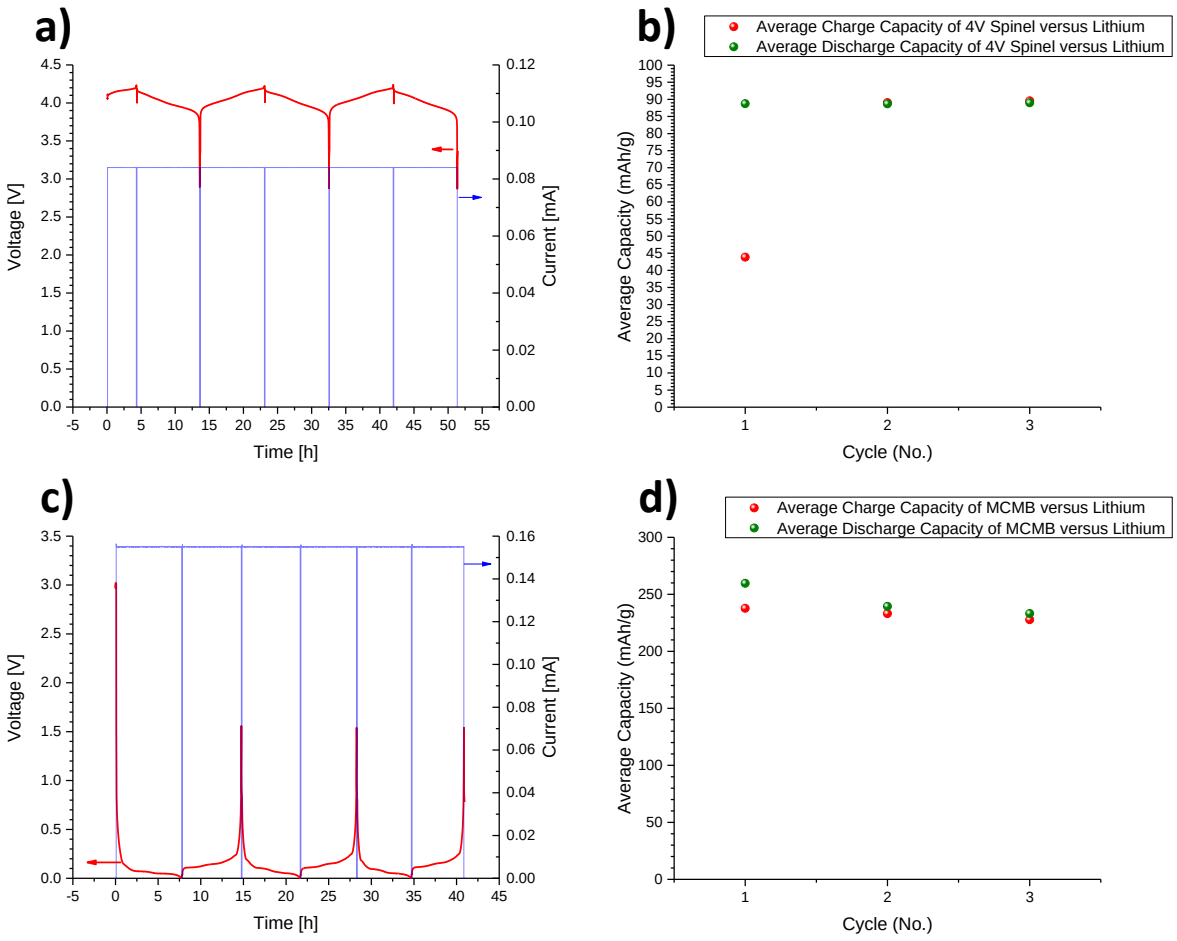

Figure 15 a) Voltage profile for faded $Li_xMn_2O_4$ electrode within half cell, b) average capacity for faded $Li_xMn_2O_4$ electrodes within half cells, c) voltage profile for faded MCMB electrode within half cell, d) average capacity for faded MCMB electrodes within half cells.

Figure 15 indicates that the faded $Li_xMn_2O_4$ electrode is missing a large amount of lithium. This effect can be seen by looking at the voltage profile (Figure 15a) or the average capacity (Figure 15b) for the first charging cycle of the faded $Li_xMn_2O_4$ electrode. In the voltage profile for the first charging cycle, the potential of the $Li_xMn_2O_4$ electrode starts at 4.1 V and then increases to 4.2 V, which indicates that a large portion of lithium is missing. This effect is also evident in the average capacity for the first charging cycle, where the charging capacity is only 44 mAh/g for

the first cycle. Given that lithium ions are moving from the cathode to the anode during the charging process, it is evident that the cathode does not possess all the lithium that it once had. After the first charging cycle, however, the faded $Li_xMn_2O_4$ electrode cycles as if it were a new $Li_xMn_2O_4$ electrode. This finding indicates that once the lithium in the faded $Li_xMn_2O_4$ electrode is replenished, it is able to cycle with its full capacity. Next, Figure 15c shows the voltage profile of the graphite begins at 3 V which implies that the graphite is fully de-lithiated. Thus, the missing lithium is not in the graphite electrode. Lastly, Figure 15d shows that the faded graphite electrode operates with a slightly diminished capacity which implies that the electrode has a small interfacial impedance.

The results from these experiments indicate that the primary contributor to the capacity fade within the $Li_xMn_2O_4$ and graphite cell is a loss of lithium from the normal operation of the cell and not a dramatic increase in the internal resistance. Thus, the next question is, How does the dissolution of the manganese remove lithium from the normal operation of the cell? Our hypothesis is that the manganese ions deposit onto the outer surface of the inner SEI layer, which is known to be a mixture of inorganic salts (e.g., Li_2CO_3, LiF, and Li_2O) [41-44]. In this location, the manganese is reduced from an oxidation state of 2 [49, 52] to an oxidation state of 1 during the lithiation of the graphite [52, 53] by an electron that transports from the graphite to the manganese, likely through the grain boundaries of the inner SEI layer. Since the manganese is on the outer surface of the inner SEI layer, the manganese can coordinate an ethylene carbonate molecule, and then transfer an electron to this coordinated ethylene carbonate molecule. In doing so, the ethylene carbonate molecule decomposes into lithium ethylene di-carbonate ($(CH_2OCO_2Li)_2$) [42, 43, 54] and thereby removes the lithium from the normal operation of the cell (see Figure 16).

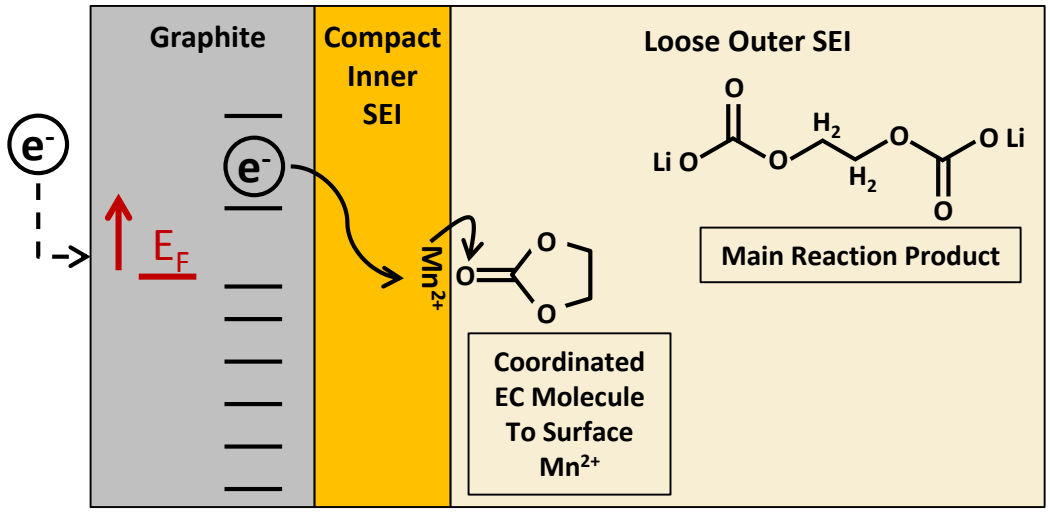

Figure 16 Diagram to illustrate our hypothesis.

A number of key points should be elucidated at this juncture. First, given previous X-ray absorption fine structure spectroscopy (XAFS) measurements [49, 52], the manganese on a de-lithiated graphite anode is known to have an oxidation state of 2. Second, given similar work [52, 53], the manganese on a lithiated graphite anode is known to hold an unknown "reduced" oxidation state. Shkrob et al. went to great lengths to demonstrate that manganese is not in an oxidation state of 0 and conjectured that manganese is likely in a reduced oxidation state of 1 [52]. Next, another key point is the electron transporting across the inner compact SEI layer via grain boundaries. The transport of electrons through tens of nanometers or even hundreds of nanometers via grain boundaries is not peculiar. For instance, ultra-nano-crystalline diamond (UNCD) is known to transform from an insulator to an electrical conductor when the extent of the grain boundaries in the material is increased by reducing the size of the crystallite [55]. In the case of UNCD, doping the grain boundaries with nitrogen dramatically increases the electrical conduction [56, 57]. Other materials such as lithium peroxide (Li_2O_2) have similar behaviors. For instance, DFT calculations performed on amorphous Li_2O_2, which is likely present in the Li_2O_2 grain boundaries, reveal that amorphous Li_2O_2 may have a metal-like density of states [58]. The electrical conductivity of the grain boundaries is related to the amorphous nature of the grain boundaries. Thus, grain boundaries can play a significant role in the electrical properties of materials. Therefore, we believe that the electrons are able to transport through the inner compact SEI layer via the grain boundaries. With respect to the mobility of the ethylene carbonate, it should be noted that the ethylene carbonate molecule is able to move through the loose outer SEI

layer yet is unable to move through the inner SEI [59]. As a result, the ethylene carbonate is able to reach the outer surface of the inner SEI. Lastly, the lithium ethylene di-carbonate is unstable and likely decomposes via various routes dependent upon what chemical species are in near proximity when it is formed. For instance, lithium ethylene di-carbonate can decompose into lithium carbonate, Li_2CO_3, and ethylene gas, C_2H_4, or it can polymerize into long polymer chains. In summary, our hypothesis accounts for all of these key points.

Next, a number of experiments to test our hypothesis were devised. First, if the hypothesis is correct, then a graphite electrode with a pristine SEI should be poisoned by an electrolyte containing manganese ions. Thus, MCMB graphite electrodes in half cells were cycled for three cycles at a C/10 rate to form a pristine SEI on the MCMB graphite. Then, the MCMB graphite electrodes were harvested from the half cells and soaked in a GEN 2 Electrolyte with a concentration of approximately 44 μg/g of manganese over-night within a glove box. The concentration of manganese was determined via ICP-MS analysis. The soaked MCMB graphite electrodes were then assembled into coin cells with fresh $Li_{1-\delta}Mn_2O_4$ electrodes. These coin cells were compared against coin cells with fresh $Li_{1-\delta}Mn_2O_4$ electrodes and fresh MCMB graphite electrodes by cycling them at room temperature.

Figure 17 presents the results of this comparison.

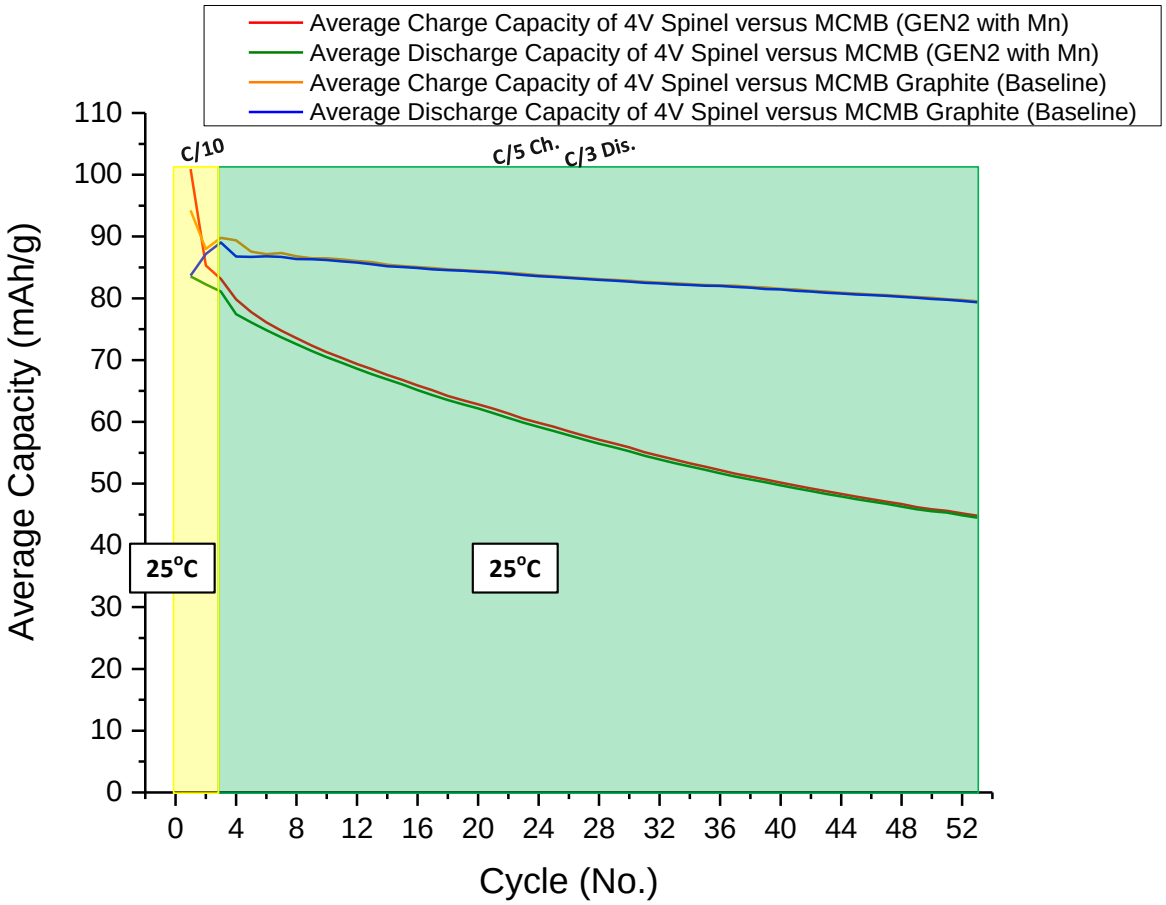

Figure 17 Average capacity for cell with $LiMn_2O_4$ cathode and MCMB graphite anode after the MCMB graphite is soaked in GEN2 Electrolyte with Mn^{2+}.

Figure 17 demonstrates that the fading of the coin cell can be artificially induced by soaking the graphite electrode with a pristine SEI in an electrolyte containing manganese ions. This experimental result begins to substantiate the hypothesis.

Given that soaking the graphite electrode with a pristine SEI in an electrolyte containing manganese ions induces the capacity fading, an inkling that the manganese is reacting with the SEI layer on the graphite electrode begins to emerge. From the hypothesis, the manganese ions in the electrolyte should react with one or more of the primary constituents of the inner inorganic SEI layer, namely carbonate (Li_2CO_3), lithium fluoride (LiF), and lithium oxide (Li_2O). To confirm this assertion, theoretical calculations and targeted experiments were run.

5.3 Theoretical and experimental results

The results of the gas phase density functional theory (DFT) calculations of reactions of Mn^{2+} ion in the ethylene carbonate (EC) complexes with Li_2CO_3, Li_2O, and LiF are in Table 4.

Table 4: DFT Results

Gas Phase Reaction	Free Energy ΔG_{gas} (eV)
$Li_2CO_3 + [Mn(EC)_6]_2^+ + 2EC = 2[Li(EC)_4]^+ + MnCO_3$	-1.33
$Li_2CO_3 + [Mn(EC)_6]_2^+ + 2EC = 2[Li(EC)_4]^+ + MnO$	-3.33
$2LiF + [Mn(EC)_6]_2^+ + 2EC = 2[Li(EC)_4]^+ + MnF_2$	-4.83

From Table 4, the DFT calculations predict that each of the primary constituents of the inner inorganic SEI layer will sequester the manganese ions from the electrolyte. Although these calculations are approximate since they represent molecular reaction energies and not solid phase reactions, these results bolster the hypothesis that the manganese ions can exchange with the lithium on the outer surface of the inner inorganic SEI layer.

Next, to determine if the primary constituents of the inner SEI actually sequester the Mn^{2+} ions from the GEN 2 Electrolyte, a straight forward experiment that utilized ICP-MS to measure the concentration of manganese ions in the electrolyte given varying conditions was designed. The experiment involved taking the GEN2 Electrolyte with a known concentration of manganese ions and adding 0.5 grams of each of the known constituents of the inner SEI. The electrolyte was then stirred overnight in an argon atmosphere glove box. Finally, ICP-MS was utilized to measure the change in the concentration of the manganese ions in the electrolyte. The ICP-MS results are in Table 5.

Table 5: ICP-MS results

Electrolyte	Mn Concentration $\left(\mu g/g\right)$	Mn Concentration $\left(\mu g/ml\right)$
Pristine GEN 2	0.005	0.006
GEN 2 with Mn^{2+}	38.700	46.900
GEN 2 with Mn^{2+} with LiF	8.850	10.600
GEN 2 with Mn^{2+} with Li_2O	0.039	0.046
GEN 2 with Mn^{2+} with Li_2CO_3	0.026	0.031

The results reveal that each of the primary constituents of the inner inorganic SEI layer is able to sequester manganese ions from the electrolyte. Notably, lithium carbonate, Li_2CO_3, drops the concentration of manganese ions from 38.700 μg/g to 0.026 μg/g which represents a reduction by a factor of 1,488 or greater than three orders of magnitude.

Now that the theoretical and experimental work demonstrated that each of the primary constituents of the inner inorganic SEI layer is able to sequester manganese ions from the electrolyte, the next logical step is to measure the leakage current that is caused by the parasitic reactions between the graphite and the electrolyte at various potentials holding the temperature at 30°C.

5.4 Characterization of parasitic reactions

To determine if an MCMB electrode that has been exposed to manganese ions in the electrolyte through the cycling of a full cell at 55℃ (i.e. the faded MCMB electrode) increases the reduction rate of electrolyte as compared to an MCMB electrode that has not been exposed to the manganese ions in the electrolyte (i.e. the formation MCMB electrode), steady-state current measurements were taken at varying potentials at 30°C. These measurements are based upon the current and forward rate constant relationships that were discussed back in Chapter 2 namely Equations 1 through 4.

From Equations 2, 3a, 3b, and 4, it is clear that the steady-state current in our half cells taken at various potentials versus $Li^+/Li(s)$ is dependent upon a number of coefficients and variables. The objective of our work is to determine if any significant difference in the steady-state current exists between the faded MCMB graphite electrode and the formation MCMB graphite electrode at varying potentials holding the temperature constant at 30°C. Any significant difference in the steady-state current between these electrodes will provide evidence that their kinetic behavior is different.

To this end, half cells with faded MCMB graphite and formation cycled MCMB graphite cathodes, and metallic lithium anodes were fabricated and placed into the ERKAS for evaluation. The operating temperature of the half cells was held constant while the potential was stepped through the following sequence: 1.2V, 1.1V, 1.0V, 0.9V, 0.8V, 0.7V, 0.6V, 0.5V, 0.4V, 0.3V,

0.2V, 0.1V, and 0.0V. The corresponding steady-state currents were then measured. The results are found in Figure 18.

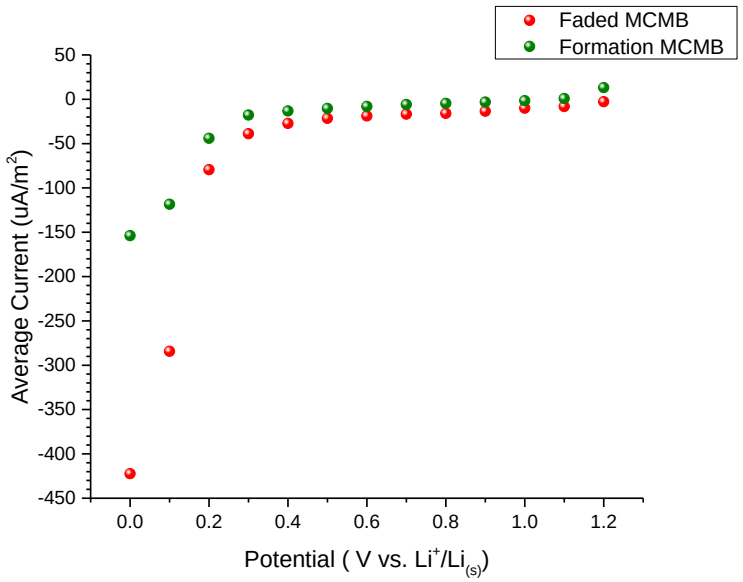

Figure 18 Steady-state results for interfacial reactions: Faded MCMB and Formation Cycled MCMB.

From Figure 18, a key result emerges. The steady-state currents at the lower potentials are dramatically higher for the faded MCMB electrode than for the formation MCMB electrode. Thus, the presence of manganese in the Li-ion cell dramatically increases the reduction rate of the GEN 2 Electrolyte.

The increase in the steady-state current can be attributed to likely changes in a number of factors. For instance, the presence of manganese on the outer surface of the inner inorganic SEI layer likely reduces the work to move the reactant to the reaction location from the average environment, w_O, in Equations 3a and 3b. As a result, the activation energy for the reduction of O, $\Delta G_f^{\ddagger}$, is likely reduced leading to an increase in the steady-state current. The other factors that could explain the increase in the steady-state current are an increase in the pre-exponential factors. For example, the presence of manganese could increase the nuclear frequency and/or the electronic transmission coefficient which would lead to an increase in the leakage current. Additional work is required to understand which factors are actually changing in the presence of manganese. Regardless, the presence of manganese alters the kinetics for the reduction of the electrolyte which further substantiates the hypothesis.

In an effort to test the hypothesis more thoroughly, cyclic voltammetry was used to investigate the response of the graphite electrode with a pristine SEI in an electrolyte similar to the GEN 2 electrolyte where the lithium salt, $LiPF_6$, is replaced by a manganese salt, $Mn(PF_6)_2$. In doing so, the current from lithium intercalation into the graphite is removed and only the current from the decomposition of the electrolyte is seen.

5.5 Cyclic voltammetry results

The objective in using cyclic voltammetry is to confirm that the electrolyte is decomposing on the graphite surface even though the graphite surface possesses a passivating SEI. In this experiment, the manganese salt electrolyte accomplishes two purposes. First, it removes the current associated with the intercalation of lithium ions into the graphite. Second, it provides a source of manganese ions for the SEI to exchange with. Figure 19 shows the first full cycle of our cyclic voltammetry analysis.

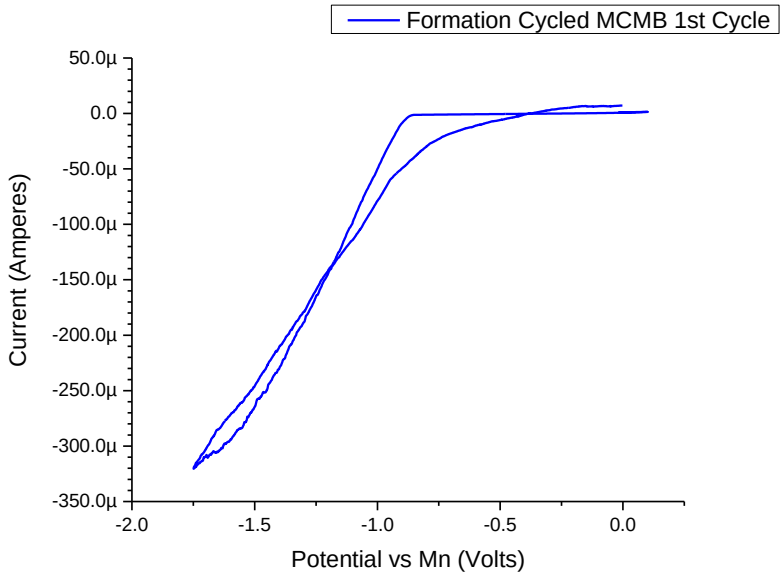

Figure 19 Cyclic voltammetry results for the first cycle of the formation cycled MCMB electrode within the manganese based salt electrolyte

Figure 19 confirms that the electrolyte is reduced on the surface of the graphite electrode even though the surface of the graphite has a passivating SEI layer. The result is also consistent with the reduction of ethylene carbonate (EC) which is known to reduce on graphite around 0.8V versus $Li^+/Li_{(s)}$ [60] which corresponds to -1.0V versus $Mn^{2+}/Mn_{(s)}$. Hence, the cyclic

voltammetry result indicates that EC is reducing on the surface of the graphite electrode even though that the graphite possesses a passivating SEI surface layer.

Next, if the hypothesis is correct, the majority of the manganese should be tens of nanometers from the surface of the graphite since the inner inorganic SEI layer is tens of nanometers thick. To assess the location of the manganese relative to the graphite, harvested faded MCMB graphite electrodes from full cells that were cycled within coins at 55℃ were sent to Evans Analytical Group® to run a TOF-SIMS analysis.

5.6 Time-of-flight secondary ion mass spectrometry results

To measure the distance between the location of manganese and the graphite surface, TOF-SIMS was used. TOF-SIMS applies a focused, pulsed particle beam of O_2 to displace chemical species on the electrode surface. The displaced species are then accelerated into a flight path on their way towards a detector. Since the "time-of-flight" of the species between the time of displacement and impact with the detector can be measured on the scale of nano-seconds, a mass resolution as fine as 0.00X atomic mass units is possible.

TOF-SIMS analysis was applied to measure the depth profile of manganese, hydrogen, carbon and lithium as a function of sputter time which is similar to work performed by Lee [61] and Abraham [45]. The analysis was done on two length scales namely a 50 μm by 50 μm length scale and a 5 μm by 5 μm length scale. The objective of using the 5 μm by 5 μm length scale was to focus on a small area of a single 15μm MCMB particle in order to improve the depth resolution of the TOF-SIMS. Figure 20 shows the TOF-SIMS results from the 50 μm by 50 μm length scale on the faded MCMB electrode where the origin, 0 nm, corresponds to the electrolyte/SEI interface or the outer most surface of the electrode.

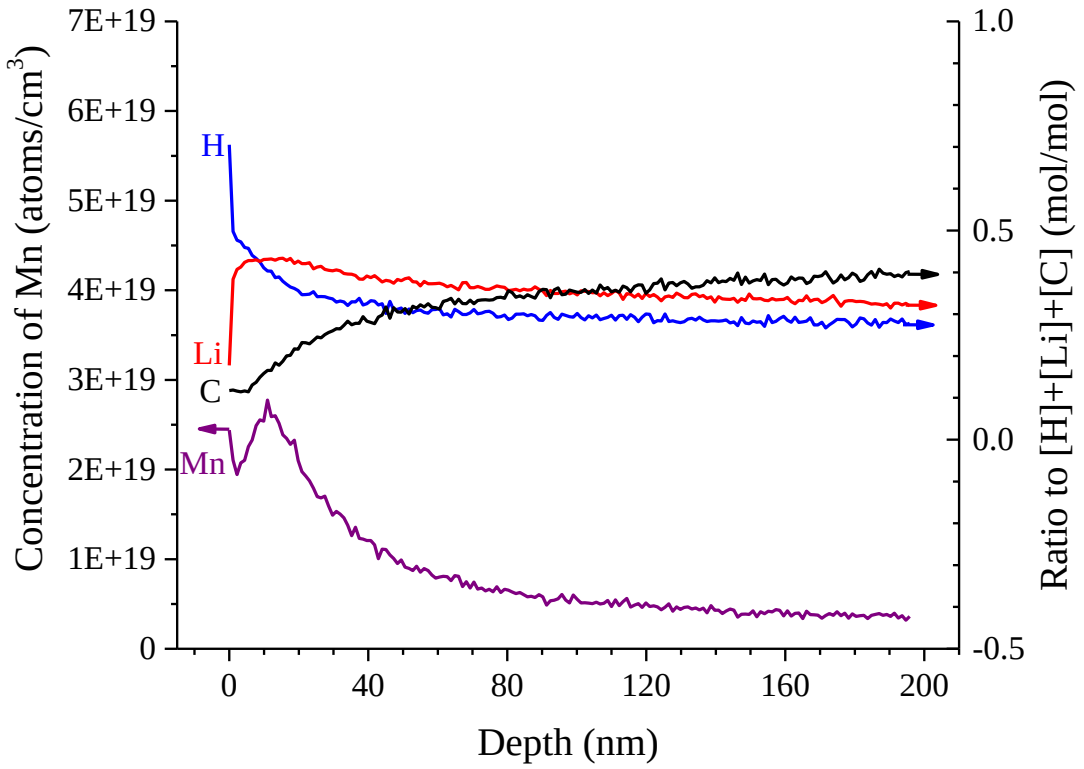

Figure 20 TOF-SIMS results Mn concentration on left y-axis and H, Li, and C composition on right y-axis versus depth in nm on a 50 μm by 50 μm length scale

Figure 20 reveals a number of discoveries. First, the hydrogen drops dramatically from the origin (i.e. the electrolyte/SEI interface) to roughly a depth of 50 nm. Second, the manganese peaks before the carbon reaches its maximum value. However at this length scale, nothing more conclusive can be determined.

Next, a shorter length scale analysis was performed in an effort to improve the resolution of the depth profile. Figure 21 illustrates the TOF-SIMS results from the 5 μm by 5 μm length scale with a 300 nm probe.

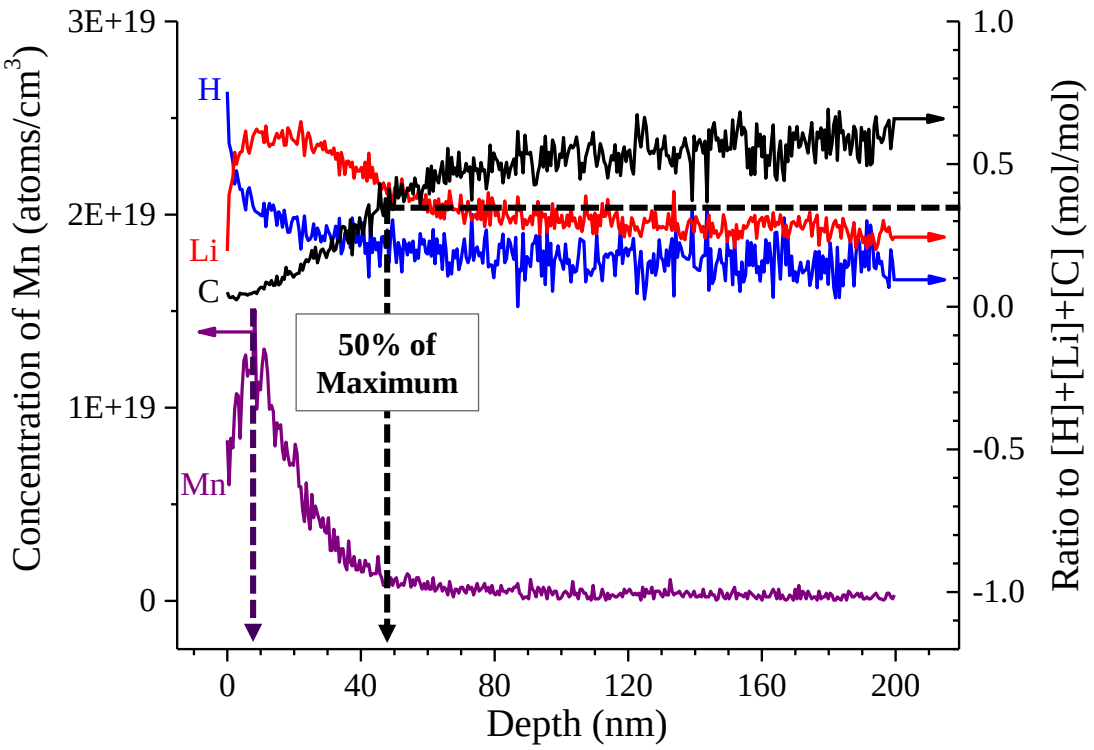

Figure 21 TOF-SIMS results Mn concentration on left y-axis and H, Li, and C composition on right y-axis versus depth in nm on a 5 μm by 5 μm length scale.

Figure 21 provides greater insights in the location of the manganese. With TOF-SIMS analysis, the boundary between differing materials is not clearly resolved, yet a rule of thumb is that the boundary is located at 50% of the maximum concentration. Thus, the surface of the graphite starts at approximately 48 nm from the electrolyte/SEI interface. The peak of the manganese is located approximately 8 nm from the electrolyte/SEI interface. Thus, the distance between the peak of the manganese and the start of the graphite surface is roughly 40 nm which is very close to the reported thickness of the inner inorganic SEI on the graphite [41].

In the literature, the prevalent model for the SEI consists of an outer layer near the electrolyte/SEI interface and an inner layer near the SEI/graphite interface. The outer layer is a loose combination of organic materials such as $(CH_2OCO_2Li)_2$ and $ROCO_2Li$ where R is an organic group that depends on the solvent [41-44, 62]. In contrast, the inner layer is a compact composition of inorganic lithium compounds such as Li_2CO_3, LiF, and Li_2O [41-44]. It should be noted that the outer layer contains hydrogen, yet the inner later does not. Thus, the dramatic drop in hydrogen before the peak of manganese in Figure 21 provides evidence that the manganese is

not located in the outer SEI layer but is located on the outer surface of the inner inorganic SEI layer (i.e. outer SEI/inner SEI interface). It should be noted that adsorbed water could account for the first 2 nm of the dramatic drop in hydrogen due to the roughness of the surface, but even if the first 2 nm of the hydrogen curve in Figure 21 is discarded, the hydrogen is still dropping before the peak in manganese.

To further test the hypothesis, X-ray photoelectron spectroscopy (XPS) with depth profiling was used to assess the bonding of the constituents within the SEI at various depths to determine the location of the manganese within the SEI which is again similar to the work done by Lee [61].

5.7 X-ray photoelectron spectroscopy results

XPS is a surface chemical analysis technique that is used to analyze the surface chemistry of materials. By irradiating a material with X-rays and determining the kinetic energy and intensity of the electrons that escape from the surface of the material, the XPS spectra are collected. Since the XPS is a surface sensitive technique, numerous argon ion milling cycles were applied to enable the measurement of an XPS depth profile. It should be noted the sputter depth of 0 nm in Figure 22 represents the outer most surface of the SEI layer (i.e. electrolyte/SEI interface).

Figure 22 shows our XPS depth profile results.

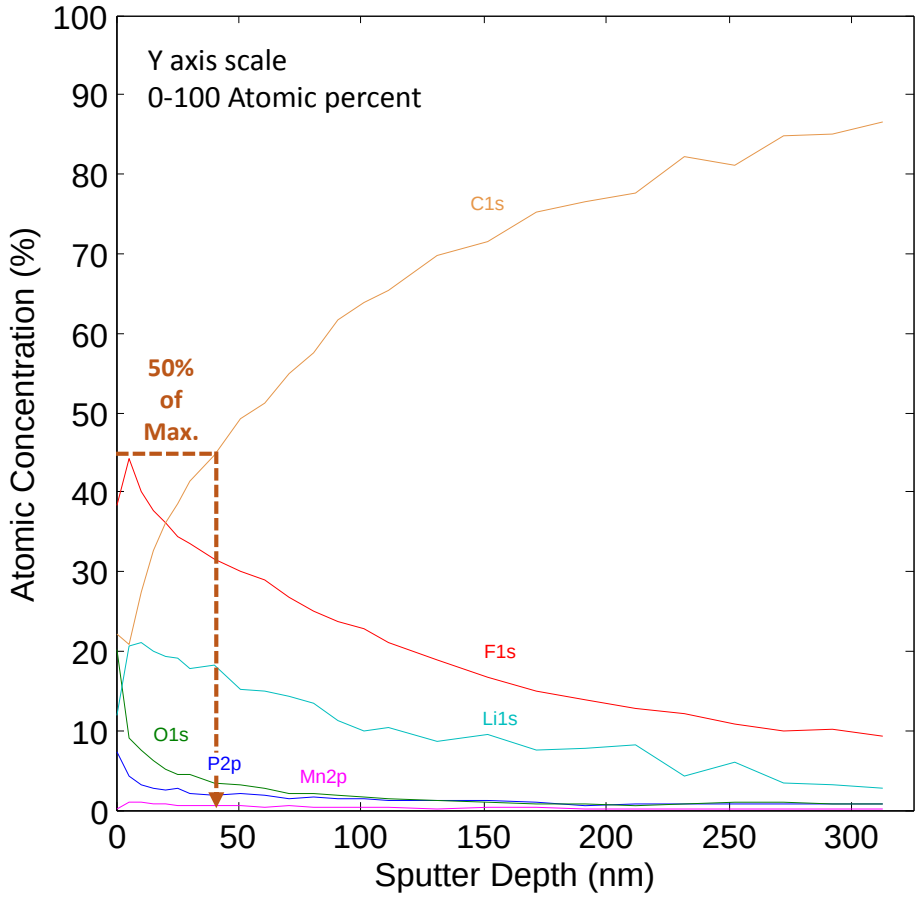

Figure 22 XPS depth profile results: C_{1s} XPS spectra

Given the rule of thumb that the boundary is positioned at 50% of the maximum concentration, the graphite surface begins at a depth of roughly 41 nm from the electrolyte/SEI interface which compares well with our TOF-SIMS results.

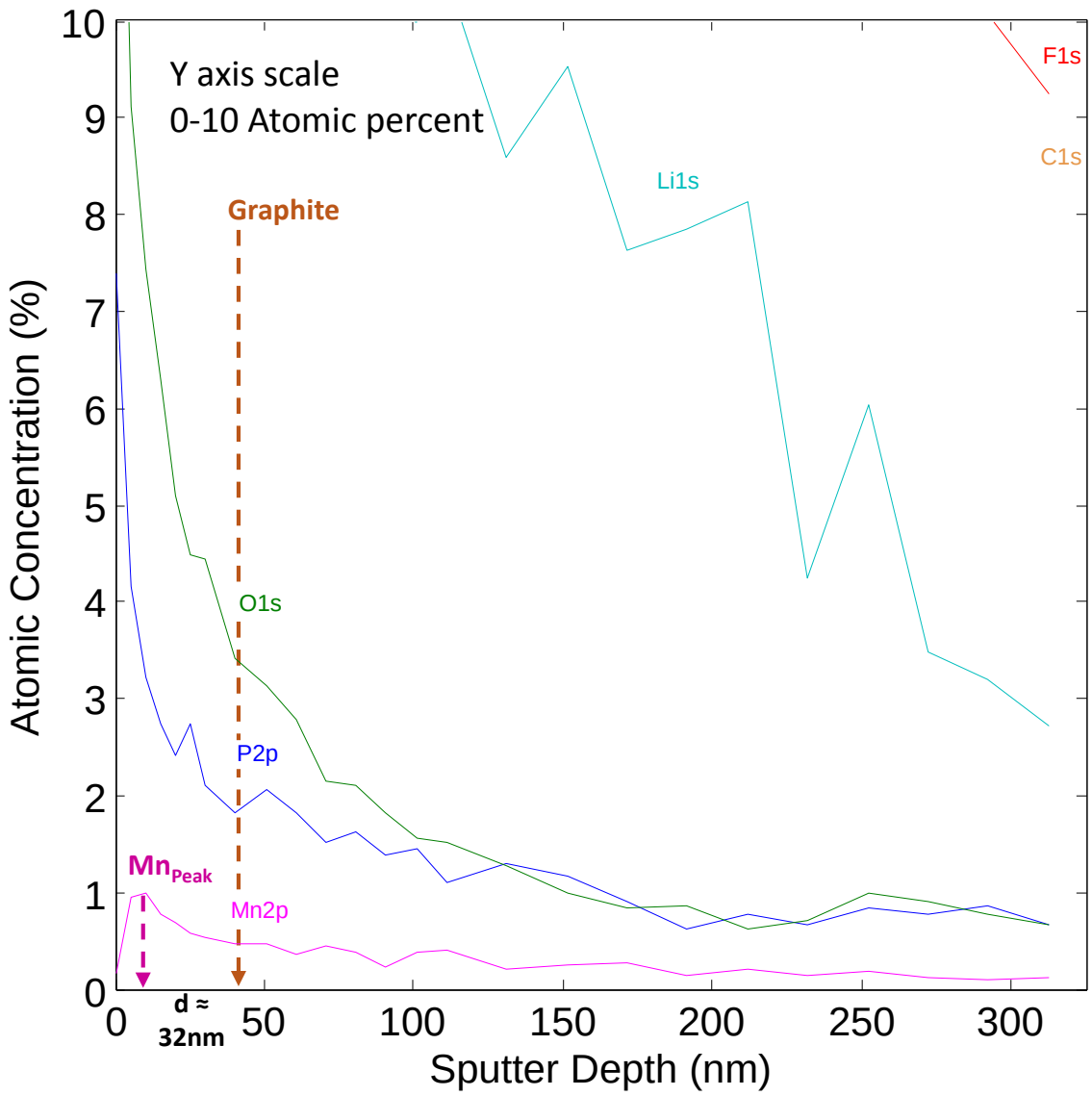

Figure 23 XPS depth profile results: Mn_{2p} and P_{2p} XPS spectra

From Figure 23, the manganese peaks at roughly 9 nm from the electrolyte/SEI interface. Thus, there exists a distance of roughly 32 nm between the peak of the manganese and the onset of the graphite surface. This result agrees well with our TOF-SIMS result which provides further evident that the manganese is located on the outer surface of the inner SEI layer (i.e. outer/inner SEI interface). Figure 23 also reveals that the concentration of phosphorus drops sharply before the manganese peaks. This phenomenon can be explained by understanding the properties of each layer of the SEI. The outer SEI layer is a loose polymeric layer through which the electrolyte transverses [59, 62]. In contrast, the inner SEI layer is a compact structure [62]

through which the electrolyte does not transverse [59]. As a result, the $LiPF_6$ salt of the electrolyte remains in the outer loose SEI layer yet does not penetrate the inner compact SEI. For this reason, the phosphorus is dropping before the peak in manganese. This XPS result strengthens our hypothesis.

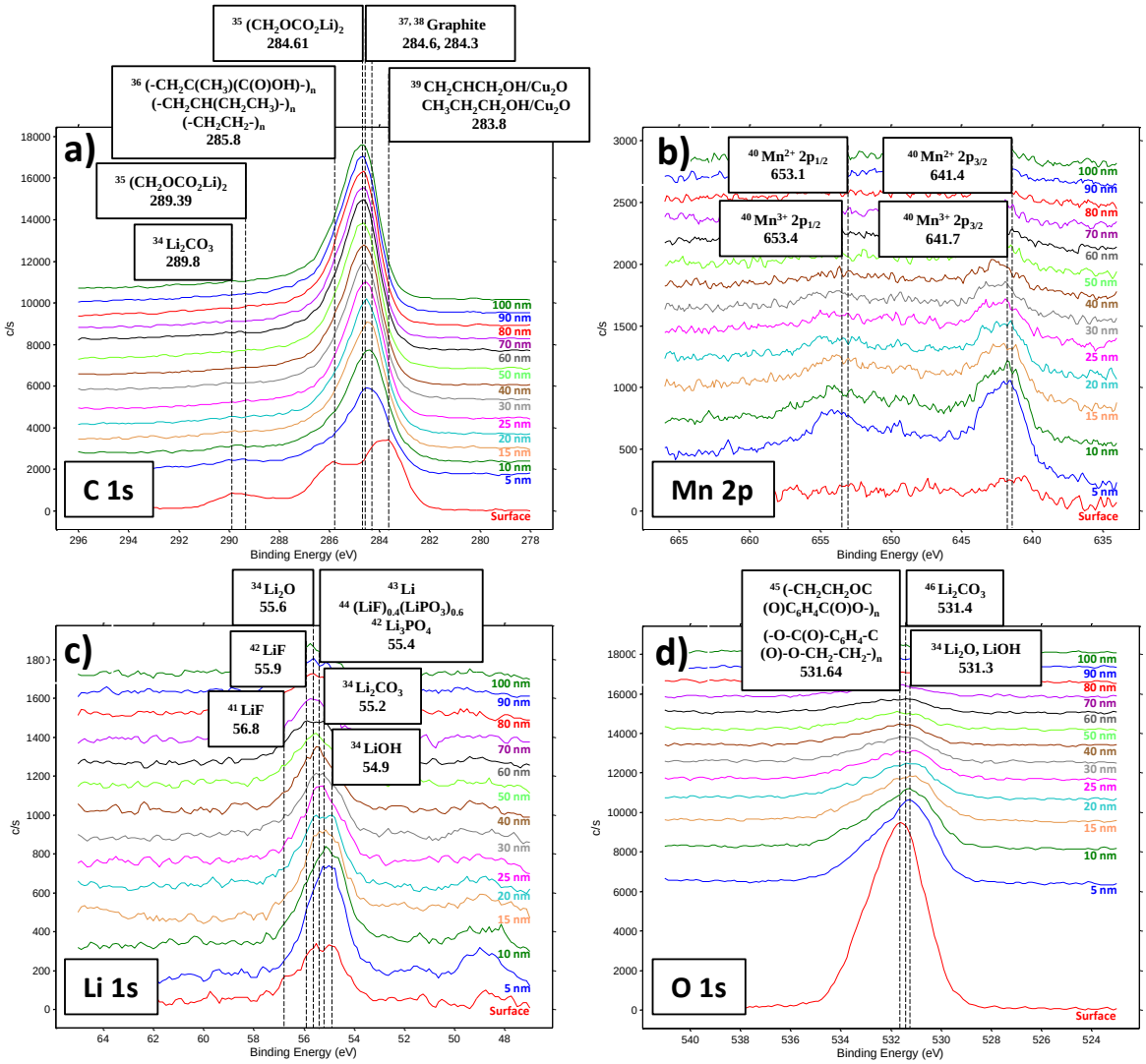

Figure 24 XPS binding energy spectra analysis: (a) C_{1s} XPS spectra, (b) Mn_{2p} spectra, (c) Li_{1s} spectra, (d) O_{1s} spectra.

Table 6: XPS Peak References

XPS Spectra	Material	Binding Energy (eV)	Reference
C 1s			
	Li_2CO_3	289.8	[63]
	$(CH_2OCO_2Li)_2$	289.39, 284.61	[64]
	$(-CH_2C(CH_3)(C(O)OH)-)_n$	285.8	[65]
	$(-CH_2CH(CH_2CH_3)-)_n$	285.8	[65]
	$(-CH_2CH_2-)_n$	285.8	[65]
	Graphite	284.6, 284.3	[66, 67]
	CH_2CHCH_2OH/Cu_2O	283.8	[68]
	$CH_3CH_2CH_2OH/Cu_2O$	283.8	[68]
Mn 2p			
	Mn^{3+} $2p_{1/2}$	653.4	[69]
	Mn^{2+} $2p_{1/2}$	653.1	[69]
	Mn^{3+} $2p_{3/2}$	641.7	[69]
	Mn^{2+} $2p_{3/2}$	641.4	[69]
Li 1s			
	LiF	56.8	[70]
	LiF	55.9	[71]
	Li_2O	55.6	[63]
	Li	55.4	[72]
	$(LiF)_{0.4}(LiPO_3)_{0.6}$	55.4	[73]
	Li_3PO_4	55.4	[71]
	Li_2CO_3	55.2	[63]
	LiOH	54.9	[63]
O 1s			
	$(-CH_2CH_2OC(O)C_6H_4C(O)O-)_n$	531.64	[74]
	$(-O-C(O)-C_6H_4-C(O)-O-CH_2-CH_2-)_n$	531.64	[74]
	Li_2CO_3	531.4	[75]
	Li_2O	531.3	[63]
	LiOH	531.3	[63]

In Figure 24, the two layer SEI model is confirmed. First, the outer polymeric layer is seen on the surface (i.e. electrolyte/SEI interface). For instance, the XPS C 1s peak at approximately 290 eV in Figure 24a is consistent with lithium ethylene di-carbonate (LEDC) that has been exposed to ambient moisture and thereby forms Li_2CO_3 [64]. In addition, the XPS C 1s peak at approximately 286 eV agrees with previously published results of cycled graphite anodes [64,

76]. The XPS C 1s peak at 283.8 eV is believed to be a product of a reaction between dissolved copper in the electrolyte from the anode current collector and the lithium ethylene di-carbonate, a key constituent of the outer polymeric SEI layer. Next, the inner inorganic layer is visible from roughly 5 nm to 40 nm in the XPS O 1s and Li 1s binding energy spectra. For instance, the constituents of the inner SEI layer are known to be Li_2CO_3, Li_2O, and LiF. The Li_2O O 1s peak (531.3 eV) and Li_2CO_3 Li 1s peak (55.2 eV) start at a depth of approximately 5 nm from the electrolyte/SEI interface and continue until approximately 40 nm which agrees with our earlier results. LiF also appears to be present in this region.

Given the manganese binding energy spectra in Figure 24b), the known peaks for Mn^{2+} $p_{1/2}$ and $p_{3/2}$ at 653.1 eV and 641.4 eV respectively [69] and Mn^{3+} $2p_{1/2}$ and Mn^{3+} $2p_{3/2}$ at 653.4 eV and 641.7 eV respectively [69], the oxidation state of manganese appears to be either 2 or 3. Using X-ray absorption fine structure (XAFS) spectroscopy, the oxidation state of manganese on un-lithiated graphite anode is reported to be 2 [49, 52]. Therefore, our XPS results are consistent with the literature. Manganese is clearly present at depths of 5 nm and 10 nm from the electrolyte/SEI interface yet fades from this point which is consist to our earlier discover that the concentration of manganese peaks at approximately 9 nm from the electrolyte/SEI interface. It is important to note that at a depth of approximately 5 nm the inner inorganic SEI layer also begins. Thus, we have additional evidence that the manganese is located on the outer surface of the inner inorganic SEI layer (i.e. outer/inner SEI interface).

Now two different analysis techniques have confirmed that the majority of manganese is located tens of nanometers from the surface of the graphite and on the outer surface of the inner inorganic SEI layer. Given that the hypothesis has been thoroughly tested, it is reasonable to conclude that the hypothesis is the best explanation for the dramatic capacity fading of Li-ion batteries utilizing manganese based cathodes and graphite anodes.

5.8 Conclusion

Through coordinated experiments, the dominate contributor to the capacity fading associated with the deposition of manganese on the graphite anode has been shown to be a removal of lithium from the normal rocking chair operation of the Li-ion battery.

To guide a deeper investigation into this phenomenon, a hypothesis was established based upon the current literature and various discussions with Argonne staff members. The hypothesis is that

the manganese ions deposit onto the outer surface of the inner inorganic SEI layer. In this location, the manganese is reduced during the lithiation of the graphite by an electron that tunnels from the graphite to the manganese likely through the grain boundaries of the thin inorganic inner SEI layer. Since the electrolyte is able to permeate through the loose outer SEI layer [59] and since the manganese is on the outer surface of the inner inorganic SEI layer, the manganese in this location can coordinate with an ethylene carbonate (EC) molecule in the electrolyte. Then once reduced, the manganese can transfer an electron to the coordinated EC molecule. In doing so, the EC molecule decomposes into lithium ethylene di-carbonate ($(CH_2OCO_2Li)_2$) and thereby removes lithium from the normal operation of the cell.

By designing and executing experiments to test the hypothesis, four key pieces of supporting evidence were obtained. First, the manganese ions react with each of the primary constituents of the inner inorganic SEI layer. Second, the deposition of manganese on the graphite anode increases the rate of the parasitic reactions between the electrolyte and the graphite. Third, the parasitic reaction is consistence with the reduction of ethylene carbonate. Finally, the manganese is located on the outer surface of the inner inorganic SEI layer.

In conclusion, the capacity fade of the graphite anode is associated with the deposition of the manganese on the outer surface of the inner inorganic SEI layer. In this position, the deposition of manganese increases the rate of the parasitic reactions between the lithiated graphite and the carbonate solvents.

CHAPTER 6

CONCLUDING REMARKS

Within this dissertation, a systematic approach to investigate interfacial reactions has been presented and applied to understand the interfacial reactions at both a cathode electrode and an anode electrode within a lithium-ion battery. The merit of understanding these interfacial reactions lies in their detrimental impact to the overall operation of the lithium-ion battery. If an understanding of an interfacial reaction that detrimentally impacts the performance of the lithium-ion battery can be attained, then an opportunity exists to dramatically improve the performance of the lithium-ion battery by slowing or stopping the interfacial reaction. For this reason, understanding interfacial reactions is importance to lithium-ion battery researchers and to the lithium-ion battery industry.

The approach outlined in this dissertation coupled electrochemical analyses with material analyses to understand interfacial reactions. The union of these analyses enabled not only an understanding of underlying chemistry of the interfacial reaction but an understanding of the physical changes to the material at the interface as well. The dual-faceted approach enables a more holistic view into the interfacial reaction.

The dual-faceted approach was first applied to understand the interfacial reaction between the electrolyte and a core-shell 5V spinel cathode material. A conventional 5V spinel cathode is able to complete approximately 30 cycles before a catastrophic failure in capacity occurs. However, the core-shell 5V spinel cathode material is able to cycle for 100 cycles with minimal capacity lose. Thus, the natural question is, "How can this core-shell material cycle so well?" The electrochemical analysis used to understand this interfacial reaction involved measuring the kinetics of the interfacial reaction. The kinetic analysis of the conventional 5V spinel, core-shell 5V spinel, and a carbon black reference was performed. The kinetic analysis demonstrated that the activation energy, $\Delta G_b^{\ddagger}$, for the oxidation of $R_{species}$ does not change between the conventional 5V spinel and the core-shell 5V spinel. The kinetic analysis also determined that the core-shell 5V spinel oxidizes more electrolyte than the 5V spinel when the surface area of each electrode is taken into account. Thus, the interfacial reaction enabling the excellent performance of the core-shell 5V spinel is not related to its ability to inhibit the oxidation of the

electrolyte. The investigation also applied two atomic scale material analyses: atom probe tomography (APT) and scanning transmission electron microscopy (STEM). These material analyses led to an understanding that a 1-2 nm nickel (II) rich layer forms on the surface of the core-shell 5V spinel that protects the structure of the core 5V spinel and thereby enabling its excellent cycling performance. It was speculated that the nickel remains in an oxidation state of 2 throughout the cycling process within the 1-2 nm nickel (II) rich layer. Since nickel in an oxidation state of 2 (i.e. nickel (II)) is more chemically stable than nickel in an oxidation state of 4 (i.e. nickel (IV)), the nickel (II) is believed to provide the chemical stability to the surface region. From this investigation, it is evident that the partnering of the electrochemical analyses with materials analyses enables a more comprehensive view into the interfacial reaction.

The dual-faceted approach was then applied to understand the interfacial reaction between the electrolyte and a graphite anode material with a deposition of manganese. The capacity fading associated with the deposition of manganese onto a graphite anode has been studied for roughly three decades. Over the past three decades, two different mechanisms to explain the capacity faded have emerged. To determine which of the two published mechanisms is the main contributor to the capacity fade, cleverly designed electrochemical cycling experiments were conducted. These experiments determined that lithium was removed from the normal operation of the battery thereby inducing the capacity fade. To understand the underlying interfacial reaction further, additional electrochemical analyses were done using measurements of the parasitic currents and cyclic voltammetry. These electrochemical analyses revealed that the deposition of manganese on the graphite anode increases the rate of reaction with the electrolyte, and the reactant in this reaction is likely ethylene carbonate. To understand the physical properties of the electrode at the interface, density functional theory (DFT) calculations, inductively coupled plasma mass spectrometry (ICP-MS), time-of-flight secondary ion mass spectrometry (TOF-SIMS) and X-ray photoelectron spectroscopy (XPS) with depth profiling were applied. These material analyses revealed the manganese ions in the GEN 2 Electrolyte react with each of the primary constituents of the inner inorganic SEI layer on the graphite. These analyses also determine that the majority of the manganese is located on the outer surface of the inner inorganic SEI layer. Thus, it was concluded that the capacity fade of the graphite anode is associated with the deposition of the manganese on the outer surface of the inner inorganic SEI layer, and in this location, the deposition of manganese increases the rate of the

parasitic reactions between the lithiated graphite and the carbonate solvents. Again, it is obvious that the union of electrochemical analyses with material analyses is a powerful approach to understanding interfacial reactions.

Now that the capability of this dual-faceted approach has been demonstrated, the emerging question is, “What are the future opportunities?” In the lithium-ion battery field, the opportunities include investigating the performance of various electrolyte additives and surface coatings in addressing interfacial reactions at both the cathode to electrolyte interface and the anode to electrolyte interface. Another important opportunity outside the realm of lithium-ion batteries is to understand the interfacial reaction between the surface of metals and water that lead to corrosion. Therefore, there are numerous opportunities to leverage the capabilities of the dual-faceted approach to more thoroughly understand interfacial reactions within lithium-ion batteries and other fields of research such as the corrosion of metal surfaces.

REFERENCES

1. Vissers, D.R., et al., *Understanding atomic scale phenomena within the surface layer of a long-term cycled 5 V spinel electrode.* Nano Energy, 2016. **19**: p. 297-306.
2. Patoux, S., et al., *High voltage spinel oxides for Li-ion batteries: From the material research to the application.* Journal of Power Sources, 2009. **189**(1): p. 344-352.
3. Yang, H., G.V. Zhuang, and P.N. Ross Jr, *Thermal stability of LiPF6 salt and Li-ion battery electrolytes containing LiPF6.* Journal of Power Sources, 2006. **161**(1): p. 573-579.
4. Yonezawa, S., M. Yamasaki, and M. Takashima, *Surface fluorination of the cathode active materials for lithium secondary battery.* Journal of Fluorine Chemistry, 2004. **125**(11): p. 1657-1661.
5. Groult, T.N.a.H., ed. *Fluorinated Materials for Energy Conversion*. 1st ed. 2005, ELSEVIER. 592.
6. Etacheri, V., et al., *Challenges in the development of advanced Li-ion batteries: a review.* Energy & Environmental Science, 2011. **4**(9): p. 3243-3262.
7. Allen J. Bard, L.R.F., *Electrochemical Methods: Fundamentals and Applications, 2nd Edition.* 2001: p. 92,117-121
8. Marcus, R.A., *On the Theory of Oxidation-Reduction Reactions Involving Electron Transfer. I.* The Journal of Chemical Physics, 1956. **24**(5): p. 966-978.
9. Marcus, R.A., *On the Theory of Electron-Transfer Reactions. VI. Unified Treatment for Homogeneous and Electrode Reactions.* The Journal of Chemical Physics, 1965. **43**(2): p. 679-701.
10. Marcus, R.A., *Electron transfer at electrodes and in solution: Comparison of theory and experiment.* Electrochimica Acta, 1968. **13**(5): p. 995-1004.
11. Marcus, R.A., *Chemical and Electrochemical Electron-Transfer Theory.* Annual Review of Physical Chemistry, 1964. **15**(1): p. 155-196.
12. MacNeil, D.D. and J.R. Dahn, *Test of Reaction Kinetics Using Both Differential Scanning and Accelerating Rate Calorimetries As Applied to the Reaction of LixCoO2 in Non-aqueous Electrolyte.* The Journal of Physical Chemistry A, 2001. **105**(18): p. 4430-4439.
13. Michael E. Brown, D.D., A.K. Galwey, ed. *Comprehensive Chemical Kinetics*. 1 ed. Vol. 22. 1980, Elsevier Science. 339.
14. Dahn, J.R., *Phase diagram of Li_xC_6.* Physical Review B, 1991. **44**(17): p. 9170-9177.
15. Myung, S.-T., et al., *Spherical core-shell Li[(Li0.05Mn0.95)0.8(Ni0.25Mn0.75)0.2]2O4 spinels as high performance cathodes for lithium batteries.* Energy & Environmental Science, 2011. **4**(3): p. 935-939.
16. Park, S.H., et al., *Synthesis of Nanostructured Li[Ni1/3Co1/3Mn1/3]O2 via a Modified Carbonate Process.* Chemistry of Materials, 2005. **17**(1): p. 6-8.
17. Lipson, A.L., et al., *Current Collector Corrosion in Ca-Ion Batteries.* Journal of The Electrochemical Society, 2015. **162**(8): p. A1574-A1578.
18. Thompson, K., et al., *In situ site-specific specimen preparation for atom probe tomography.* Ultramicroscopy, 2007. **107**(2–3): p. 131-139.
19. Becke, A.D., *Density-functional exchange-energy approximation with correct asymptotic behavior.* Physical Review A, 1988. **38**(6): p. 3098-3100.
20. Becke, A.D., *Density-functional thermochemistry. III. The role of exact exchange.* The Journal of Chemical Physics, 1993. **98**(7): p. 5648-5652.
21. Schäfer, A., C. Huber, and R. Ahlrichs, *Fully optimized contracted Gaussian basis sets of triple zeta valence quality for atoms Li to Kr.* The Journal of Chemical Physics, 1994. **100**(8): p. 5829-5835.
22. M. J. Frisch, G.W.T., H. B. Schlegel, G. E. Scuseria, M. A. Robb, J. R. Cheeseman, G. Scalmani, V. Barone, B. Mennucci, G. A. Petersson, H. Nakatsuji, M. Caricato, X. Li, H. P. Hratchian, A. F. Izmaylov, J. Bloino, G. Zheng, J. L. Sonnenberg, M. Hada, M. Ehara, K. Toyota, R. Fukuda, J. Hasegawa, M. Ishida, T. Nakajima,Y. Honda, O. Kitao, H. Nakai, T. Vreven, J. J. A. Montgomery, J. E. Peralta, F. Ogliaro, M. Bearpark, J. J. Heyd, E. Brothers, K. N. Kudin, V. N. Staroverov, R. Kobayashi, J. Normand, K. Raghavachari, A. Rendell, J. C. Burant, S. S. Iyengar, J. Tomasi, M. Cossi, N. Rega, J. M. Millam, M. Klene, J. E. Knox, J. B. Cross, V. Bakken, C. Adamo, J. Jaramillo, R. Gomperts, R. E. Stratmann, O. Yazyev, A. J. Austin, R. Cammi, C. Pomelli, J. W. Ochterski, R. L. Martin, K. Morokuma, V. G. Zakrzewski, G. A. Voth, P. Salvador, J. J. Dannenberg, S. Dapprich, A. D. Daniels, O. Farkas, J. B. Foresman, J. V. Ortiz, J. Cioslowski, and D. J. Fox, *Gaussian 09, in, EM64L-G09RevA.02 edition.* 2009.
23. Tomasi, J., B. Mennucci, and R. Cammi, *Quantum Mechanical Continuum Solvation Models.* Chemical Reviews, 2005. **105**(8): p. 2999-3094.

24. Vollmer, J.M., et al., *Reduction Mechanisms of Ethylene, Propylene, and Vinylethylene Carbonates: A Quantum Chemical Study.* Journal of The Electrochemical Society, 2004. **151**(1): p. A178-A183.
25. Alcántara, R., et al., *X-ray diffraction and electrochemical impedance spectroscopy study of zinc coated LiNi0.5Mn1.5O4 electrodes.* Journal of Electroanalytical Chemistry, 2004. **566**(1): p. 187-192.
26. Sun, Y.K., C.S. Yoon, and I.H. Oh, *Surface structural change of ZnO-coated LiNi0.5Mn1.5O4 spinel as 5 V cathode materials at elevated temperatures.* Electrochimica Acta, 2003. **48**(5): p. 503-506.
27. Sun, Y.K., et al., *Electrochemical performance of nano-sized ZnO-coated LiNi0.5Mn1.5O4 spinel as 5 V materials at elevated temperatures.* Electrochemistry Communications, 2002. **4**(4): p. 344-348.
28. Sun, Y.-K., et al., *Synthesis and Electrochemical Properties of ZnO-Coated LiNi0.5Mn1.5 O 4 Spinel as 5 V Cathode Material for Lithium Secondary Batteries.* Electrochemical and Solid-State Letters, 2002. **5**(5): p. A99-A102.
29. Zhang, Z., et al., *Fluorinated electrolytes for 5 V lithium-ion battery chemistry.* Energy & Environmental Science, 2013. **6**(6): p. 1806-1810.
30. Hu, L., K. Amine, and Z. Zhang, *Fluorinated electrolytes for 5-V Li-ion chemistry: Dramatic enhancement of LiNi0.5Mn1.5O4/graphite cell performance by a lithium reservoir.* Electrochemistry Communications, 2014. **44**: p. 34-37.
31. Hu, L., Z. Zhang, and K. Amine, *Fluorinated electrolytes for Li-ion battery: An FEC-based electrolyte for high voltage LiNi0.5Mn1.5O4/graphite couple.* Electrochemistry Communications, 2013. **35**: p. 76-79.
32. Thackeray, M.M., et al., *Electrochemical extraction of lithium from LiMn2O4.* Materials Research Bulletin, 1984. **19**(2): p. 179-187.
33. Gummow, R.J., A. de Kock, and M.M. Thackeray, *Improved capacity retention in rechargeable 4 V lithium/lithium-manganese oxide (spinel) cells.* Solid State Ionics, 1994. **69**(1): p. 59-67.
34. Jiang, X., et al., *A design strategy of large grain lithium-rich layered oxides for lithium-ion batteries cathode.* Electrochimica Acta, 2015. **160**: p. 131-138.
35. Choi, W. and A. Manthiram, *Comparison of Metal Ion Dissolutions from Lithium Ion Battery Cathodes.* Journal of The Electrochemical Society, 2006. **153**(9): p. A1760-A1764.
36. Choi, N.-S., et al., *Degradation of spinel lithium manganese oxides by low oxidation durability of LiPF6-based electrolyte at 60 °C.* Solid State Ionics, 2012. **219**: p. 41-48.
37. Nishimura, K., et al., *Spinel-type lithium–manganese oxide cathodes for rechargeable lithium batteries.* Journal of Power Sources, 1999. **81–82**: p. 420-424.
38. Pieczonka, N.P.W., et al., *Understanding Transition-Metal Dissolution Behavior in LiNi0.5Mn1.5O4 High-Voltage Spinel for Lithium Ion Batteries.* The Journal of Physical Chemistry C, 2013. **117**(31): p. 15947-15957.
39. Qiao, R., et al., *Direct evidence of gradient Mn(II) evolution at charged states in LiNi0.5Mn1.5O4 electrodes with capacity fading.* Journal of Power Sources, 2015. **273**: p. 1120-1126.
40. Abraham, D.P., et al., *Surface changes on LiNi0.8Co0.2O2 particles during testing of high-power lithium-ion cells.* Electrochemistry Communications, 2002. **4**(8): p. 620-625.
41. Shi, S., et al., *Defect Thermodynamics and Diffusion Mechanisms in Li2CO3 and Implications for the Solid Electrolyte Interphase in Li-Ion Batteries.* The Journal of Physical Chemistry C, 2013. **117**(17): p. 8579-8593.
42. Aurbach, D., et al., *The Correlation Between the Surface Chemistry and the Performance of Li-Carbon Intercalation Anodes for Rechargeable 'Rocking-Chair' Type Batteries.* Journal of The Electrochemical Society, 1994. **141**(3): p. 603-611.
43. Aurbach, D., et al., *A Comparative Study of Synthetic Graphite and Li Electrodes in Electrolyte Solutions Based on Ethylene Carbonate-Dimethyl Carbonate Mixtures.* Journal of The Electrochemical Society, 1996. **143**(12): p. 3809-3820.
44. Aurbach, D., et al., *The Study of Electrolyte Solutions Based on Ethylene and Diethyl Carbonates for Rechargeable Li Batteries: I . Li Metal Anodes.* Journal of The Electrochemical Society, 1995. **142**(9): p. 2873-2882.
45. Abraham, D.P., et al., *Evidence of Transition-Metal Accumulation on Aged Graphite Anodes by SIMS.* Electrochemical and Solid-State Letters, 2008. **11**(12): p. A226-A228.
46. Li, Y., et al., *Understanding Long-Term Cycling Performance of Li1.2Ni0.15Mn0.55Co0.1O2–Graphite Lithium-Ion Cells.* Journal of The Electrochemical Society, 2013. **160**(5): p. A3006-A3019.
47. Komaba, S., N. Kumagai, and Y. Kataoka, *Influence of manganese(II), cobalt(II), and nickel(II) additives in electrolyte on performance of graphite anode for lithium-ion batteries.* Electrochimica Acta, 2002. **47**(8): p. 1229-1239.

48. Amatucci, G., et al., *The elevated temperature performance of the LiMn2O4/C system: failure and solutions.* Electrochimica Acta, 1999. **45**(1–2): p. 255-271.
49. Zhan, C., et al., *Mn(II) deposition on anodes and its effects on capacity fade in spinel lithium manganate–carbon systems.* Nat Commun, 2013. **4**.
50. Ochida, M., et al., *Influence of Manganese Dissolution on the Degradation of Surface Films on Edge Plane Graphite Negative-Electrodes in Lithium-Ion Batteries.* Journal of The Electrochemical Society, 2012. **159**(7): p. A961-A966.
51. Esbenshade, J.L. and A.A. Gewirth, *Effect of Mn and Cu Addition on Lithiation and SEI Formation on Model Anode Electrodes.* Journal of The Electrochemical Society, 2014. **161**(4): p. A513-A518.
52. Shkrob, I.A., et al., *Manganese in Graphite Anode and Capacity Fade in Li Ion Batteries.* The Journal of Physical Chemistry C, 2014. **118**(42): p. 24335-24348.
53. Gowda, S.R., et al., *Oxidation state of cross-over manganese species on the graphite electrode of lithium-ion cells.* Physical Chemistry Chemical Physics, 2014. **16**(15): p. 6898-6902.
54. Zhuang, G.V., et al., *Lithium Ethylene Dicarbonate Identified as the Primary Product of Chemical and Electrochemical Reduction of EC in 1.2 M LiPF6/EC:EMC Electrolyte.* The Journal of Physical Chemistry B, 2005. **109**(37): p. 17567-17573.
55. Gruen, D.M., *NANOCRYSTALLINE DIAMOND FILMS.* Annual Review of Materials Science, 1999. **29**(1): p. 211-259.
56. Beloborodov, I.S., et al., *Transport properties of n-type ultrananocrystalline diamond films.* Physical Review B, 2006. **74**(23): p. 235434.
57. Bhattacharyya, S., et al., *Synthesis and characterization of highly-conducting nitrogen-doped ultrananocrystalline diamond films.* Applied Physics Letters, 2001. **79**(10): p. 1441-1443.
58. Lu, J., et al., *A nanostructured cathode architecture for low charge overpotential in lithium-oxygen batteries.* Nat Commun, 2013. **4**.
59. Lu, P. and S.J. Harris, *Lithium transport within the solid electrolyte interphase.* Electrochemistry Communications, 2011. **13**(10): p. 1035-1037.
60. Imhof, R. and P. Novák, *In Situ Investigation of the Electrochemical Reduction of Carbonate Electrolyte Solutions at Graphite Electrodes.* Journal of The Electrochemical Society, 1998. **145**(4): p. 1081-1087.
61. Lee, J.T., et al., *Comparative study of the solid electrolyte interphase on graphite in full Li-ion battery cells using X-ray photoelectron spectroscopy, secondary ion mass spectrometry, and electron microscopy.* Carbon, 2013. **52**: p. 388-397.
62. Cresce, A.v., et al., *In Situ and Quantitative Characterization of Solid Electrolyte Interphases.* Nano Letters, 2014. **14**(3): p. 1405-1412.
63. Contour, J.P.S., A.; Froment, M.; Garreau, M.; Thevenin, J.; Warin, D. , *Analysis by electron microscopy and photoelectron spectroscopy of lithium surfaces polarized in anhydrous organic electrolytes.* Journal de Microscopie et de Spectroscopie Electroniques, 1979. **4**(4): p. 483-491.
64. Xu, K., et al., *Syntheses and Characterization of Lithium Alkyl Mono- and Dicarbonates as Components of Surface Films in Li-Ion Batteries.* The Journal of Physical Chemistry B, 2006. **110**(15): p. 7708-7719.
65. Watts, J.F., *High resolution XPS of organic polymers: The Scienta ESCA 300 database. G. Beamson and D. Briggs. 280pp., £65. John Wiley & Sons, Chichester, ISBN 0471 935921, (1992).* Surface and Interface Analysis, 1993. **20**(3): p. 267-267.
66. Taylor, J.A., G.M. Lancaster, and J.W. Rabalais, *Surface alteration of graphite, graphite monofluoride and teflon by interaction with Ar+ and Xe+ beams.* Applications of Surface Science, 1978. **1**(4): p. 503-514.
67. Witek, G., et al., *Interaction of platinum colloids with single crystalline oxide and graphite substrates: a combined AFM, STM and XPS study.* Catalysis Letters. **37**(1): p. 35-39.
68. Schulz, K.H. and D.F. Cox, *Oxidation, reduction, and isomerization of allyl alcohol and 1-propanol over cuprous oxide(100).* The Journal of Physical Chemistry, 1993. **97**(3): p. 647-655.
69. Tan, B.J., K.J. Klabunde, and P.M.A. Sherwood, *XPS studies of solvated metal atom dispersed (SMAD) catalysts. Evidence for layered cobalt-manganese particles on alumina and silica.* Journal of the American Chemical Society, 1991. **113**(3): p. 855-861.
70. Ro, C.u. and R.W. Linton, *Characterization of LiF Using XPS.* Surface Science Spectra, 1992. **1**(3): p. 277-283.
71. Morgan, W.E., J.R. Van Wazer, and W.J. Stec, *Inner-orbital photoelectron spectroscopy of the alkali metal halides, perchlorates, phosphates, and pyrophosphates.* Journal of the American Chemical Society, 1973. **95**(3): p. 751-755.

72. Shek, M.L., et al., *A soft X-ray study of the interaction of oxygen with Li.* Surface Science, 1990. **234**(3): p. 324-334.
73. Chowdari, B.V.R., et al., *Electrical and structural studies of lithium fluorophosphate glasses.* Solid State Ionics, 1995. **76**(3–4): p. 189-198.
74. Beamson, G., et al., *Effect of Crystallinity on the XPS Spectrum of Poly(Ethylene Terephthalate).* Surface Science Spectra, 1994. **3**(4): p. 357-365.
75. Contarini, S. and J.W. Rabalais, *Ion bombardment-induced decomposition of Li and Ba sulfates and carbonates studied by X-ray photoelectron spectroscopy.* Journal of Electron Spectroscopy and Related Phenomena, 1985. **35**(2): p. 191-201.
76. Xu, K., et al., *Chemical Analysis of Graphite/Electrolyte Interface Formed in LiBOB-Based Electrolytes.* Electrochemical and Solid-State Letters, 2003. **6**(7): p. A144-A148.
77. Gomer, R. (1961) *Field Emission And Field Ionization*. Harvard Monographs In Applied Science Number 9.

APPENDIX A

ATOM PROBE TOMOGRAPHY (APT) SPECIMEN PREPARATION

To perform APT analysis on a specimen, the specimen must first be sharpened into a nanoscale tip so that a sufficiency large electric field can be attained to ionize and remove atoms from the surface. The electric field at the apex of the tip can be approximated with the following equation [77]:

$$\overrightarrow{E_r} = \frac{V}{g_f R_t} \tag{16}$$

In the above equation, V is the electrical potential applied to the tip. $g_f$is a geometric correction factor, and $R_t$is the radius of the tip. Hence, controlling the radius of the specimen is critical for successful atom probe analysis. The strong electric field at the apex of the tip is required to induce field evaporation of atoms from their lattice positions. The field evaporation of atoms involves the ionization and desorption from the surface. To control the field evaporation process, the APT system governs the electrical potential applied to the tip and then introduces a short pulse of electrical potential to the tip or a short pulse of UV-laser energy to the tip. The pulse of energy is analogous to reaction kinetics in chemistry. The pulse of energy provides a sufficient amount of energy to overcome the forward reaction barrier or in the atom probe case, to free the atom from the surface. Once the ionized atom is freed from the surface, the strong electric field accelerates the ionized atom towards the detector. Given the acceleration potential and the time of flight of ionized atom between the energy pulse and the ionized atom hitting the detector, the mass of the ionized atom can be determine. This process is known as time-of-flight mass spectrometry. Hence, the APT system is capable of determining what type of atom hits the detector. The APT system uses a 2D detector to resolve the trajectory of the ionized atom which aids in establishing the original position of the atom. As a result, the APT system is able to reconstruct the original tip atom by atom. For a more through explanation of atom probe tomography, the interested reader is referred to Atom Probe Microscopy by Baptiste Gault, Michael P. Moody, Julie M. Cairney, and Simon P. Ringer.

To analyze the cobalt stabilized 5V spinel using APT, a number of steps were taken to form a nanoscale tip which follow similar procedures found in the literature [18]. The first step is to coat

the electrode surface with a protective deposition of nickel. The nickel deposition protects the electrode surface from ion induced damage during subsequent milling steps. The nickel coating was applied to the electrode surface using an ion beam sputter deposition system at Northwestern University. The nickel deposition is roughly 50 nm thick. This nickel deposition has trace amounts of aluminum which aid in determining the extent of the protective nickel layer in the latter APT analysis. Figure 25 and 26 are scanning electron microscopy (SEM) images of the un-cycled cobalt stabilized 5V spinel surface.

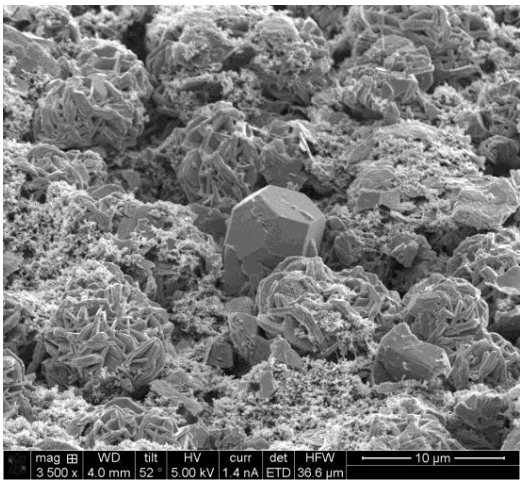

Figure 25 Surface of the un-cycled cobalt stabilized 5V spinel

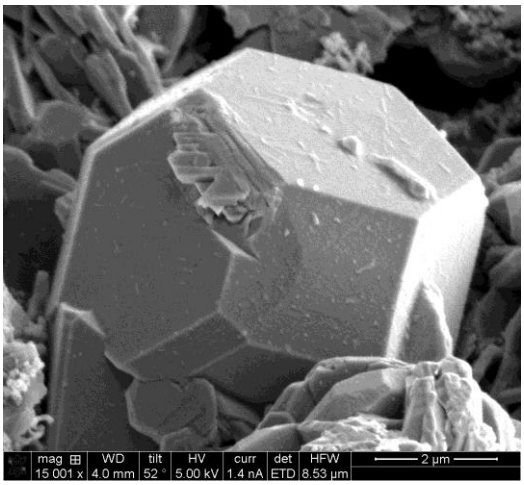

Figure 26 Surface of the un-cycled Cobalt stabilized 5V spinel

After the deposition of the nickel layer is complete, the next step in the fabrication process is to coat a section of the electrode surface with platinum using ion-beam induced deposition within a focused ion-beam (FIB) system.

Figure 27 illustrates the result of the platinum deposition on the surface of the electrode.

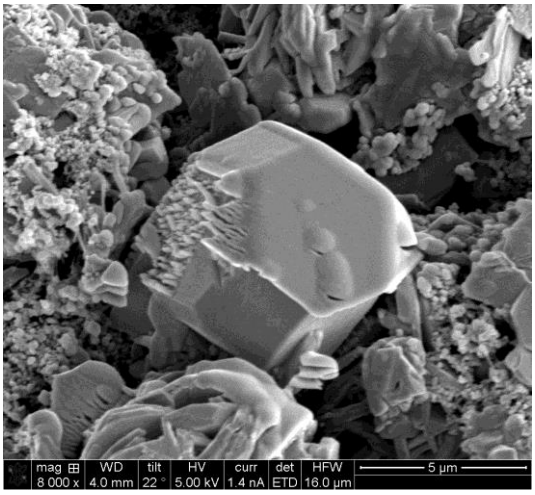

Figure 27 Surface of the un-cycled cobalt stabilized 5V spinel after Pt deposition

The next step in the process is to cut a region of interest from the surface. Figure 28 is a SEM image of the surface after the first cut into the electrode surface using the Ga+ ion milling capability of the FIB.

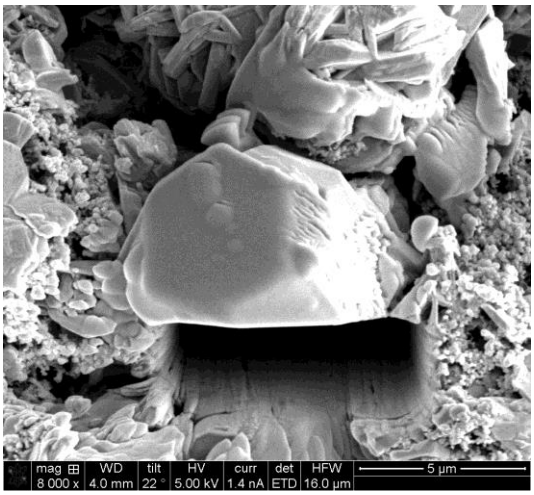

Figure 28 Surface of the un-cycled cobalt stabilized 5V spinel after cut

Additional cuts are made using the Ga+ ion milling capability of the FIB as seen in Figure 29.

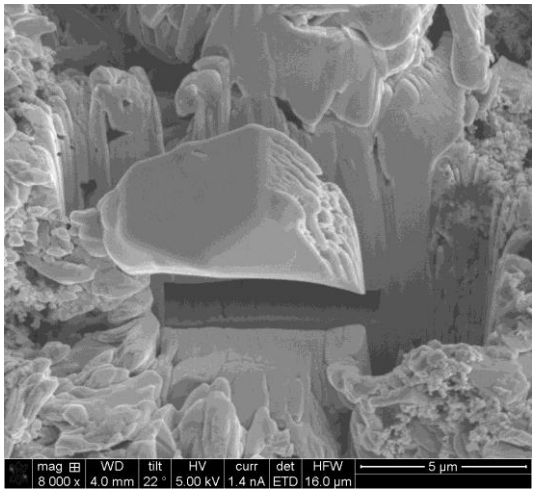

Figure 29 Surface of the un-cycled cobalt stabilized 5V spinel after additional cuts

After the additional cuts, an omni-probe needle is placed on the cut-out and a platinum deposition between the specimen and needle is formed as illustrated in Figure 30.

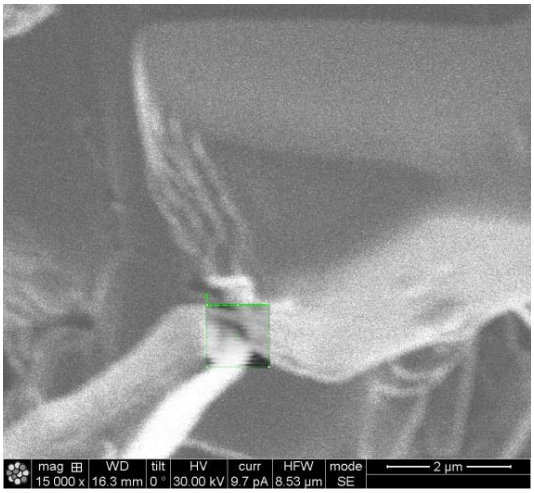

Figure 30 Attachment of needle to specimen

Once the needle is attached to the specimen, an additional cut is made to free the

specimen from the electrode. The specimen is then moved to a micro-tip array. The specimen is then positioned on one of the micro-tip array posts. Next, platinum deposition is applied to bond the specimen to one of the posts of the micro-tip array as seen in Figure 31.

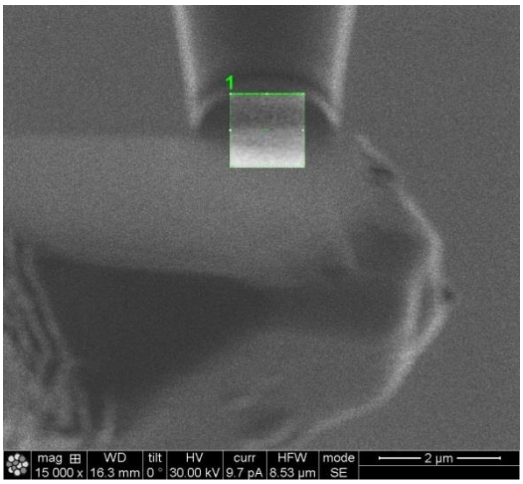

Figure 31 Attachment of the specimen to one of the posts of the micro-tip array

The excess portions of the specimen are then removed using Ga+ ion milling. The specimen at this stage in the process appears in Figure 32.

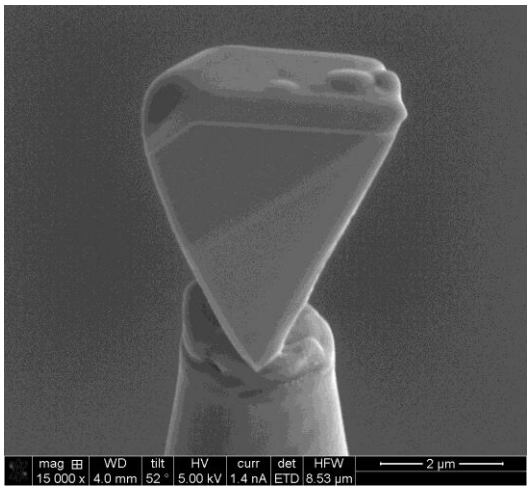

Figure 32 Specimen with an upper most Pt capping layer followed by thin nickel layer followed by the upper most region of the cobalt stabilized 5V spinel

Once the specimen is mounted on the micro-post, the next step is to mill angular cuts into the specimen to form a pyramidal foundation for the nano-tip. The pyramidal foundation fosters mechanical strength and good heat transfer capabilities between the yet to be formed nano-tip and the micro-post.

The mechanical and heat transfer properties of the nano-tip are important for the nano-tip's survival in the extreme environment of the APT system where electric field strengths easily reach 45 V/nm and higher.

After the pyramidal cuts are completed, the specimen has the form as seen in Figure 33.

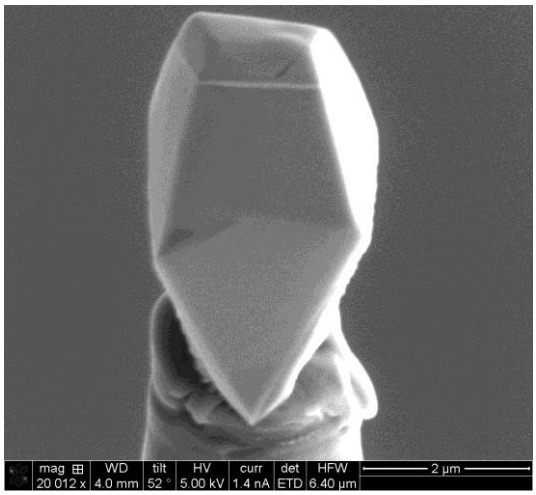

Figure 33 Specimen after pyramidal cuts

Subsequently, the specimen undergoes a two stage sharpening process utilizing special stream files provided by CAMECA. The FIB system uses these stream files to precision mill the specimen to a nano-tip. The first stage of milling results in a specimen tip as shown in Figure 34.

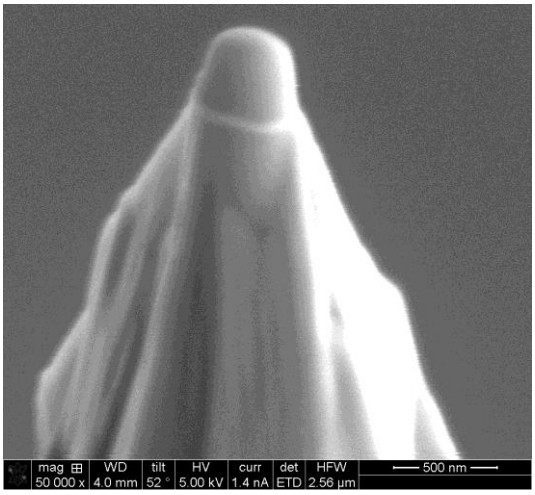

Figure 34 Specimen after first stage of milling

Next, a second stage of milling sharpens the tip closer to its final shape. Finally, the tip is polished using a low energy Ga+ ion beam to remove damage from the surface region of the tip and to leave a relatively undamaged surface for the atom probe analysis.

The final tip is shown in Figure 35.

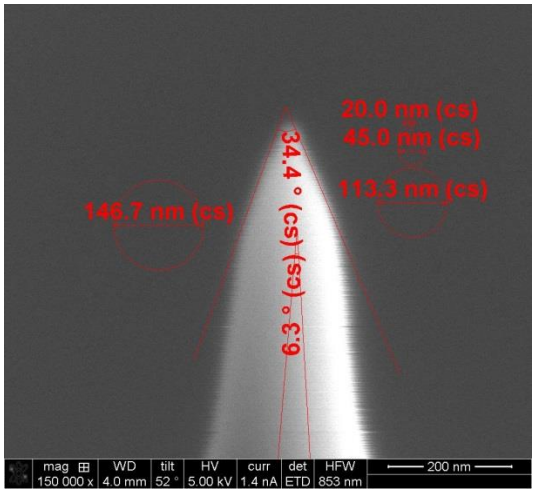

Figure 35 Final Tip

This completes the tip sharpening procedure.

APPENDIX B

INTERNAL RESISTANCE AND CAPACITY FADE RELATIONSHIP

This appendix explains the relationship between the internal resistance and the associated capacity fade within a battery. The modeling of various interfaces within electrochemical cells using electrical circuit elements is a challenge and unfortunately, a subject of much debate. But given Thevenin's theorem of circuit analysis, every electrical circuit can be simplified to an equivalent circuit with a real resistive element and an imaginary reactance element. The resistive element models Ohmic loss or heat energy dissipated in a circuit, and the reactance element models the energy stored in an electric or magnetic field. Fortunately, batteries typically operate in a DC mode where the reactance elements are either an open-circuit in the case of a capacitive reactance or a short circuit in the case of an inductive reactance. Therefore, only the resistive elements need to be considered in a DC mode of operation.

In an electrochemical cell where Mn^{2+} ions cause an increase in the impedance of the SEI, this effect can be modelled in a DC mode by an increase in the resistive element, $R_{internal}$. Hence, the circuit model illustrated in Figure 36 applies.

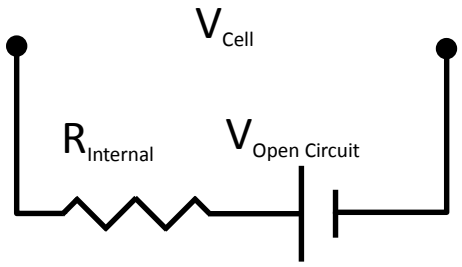

Figure 36

The internal Ohmic potential drop, $R_{internal} \times I_{xx}$, across $R_{internal}$ always works against the desired charge state of the battery.

For instance, when discharging the battery to a fixed potential, the internal Ohmic potential loss keeps the battery from reaching its fully discharged state as seen in Figure 37a. Additionally, when charging the battery to a set potential, the internal Ohmic potential loss stops the battery from reaching its fully charged state as shown in Figure 37b.

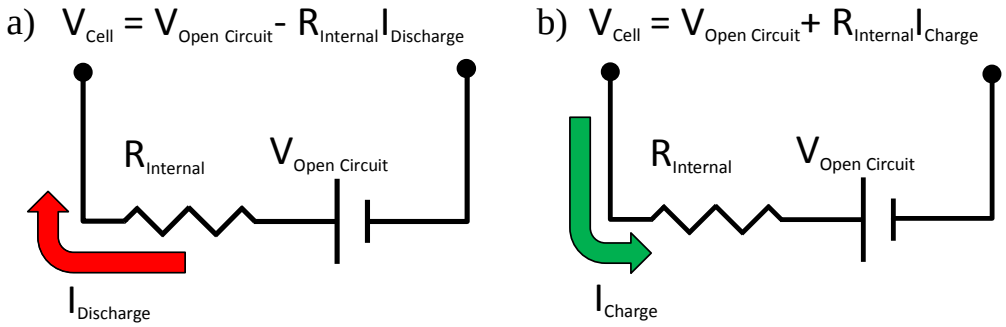

Figure 37 a) discharging state, b) charging state

$$Q_{Discharge} = \int_{V_{initial}}^{V_{Cell} = V_{Open\ Circuit} - R_{Internal} I_{Discharge}(reached\ early)} Idt \quad (17)$$

$$Q_{Charge} = \int_{V_{initial}}^{V_{Cell} = V_{Open\ Circuit} + R_{Internal} I_{Discharge}(reached\ early)} Idt \quad (18)$$

Equations 17 and 18 illustrate the same point where Q is the capacity of the cell.

Since the internal Ohmic potential drop across $R_{internal}$ is $R_{internal} \times I_{xx}$ by Ohm's Law, the capacity fade due to an increase in the internal impedance of a cell will inherently be dependent upon the charge or discharge current, I_{xx}. Therefore, by altering the charge or discharge current, I_{xx}, the capacity fade due to an increase in internal impedance can be altered. If the capacity fade is not dependent on the charge or discharge current, then the capacity fade is not related to an increase in internal impedance. Thus, changing the charge or discharge current while measuring how the capacity responds is a powerful diagnostic tool to determine the root cause for a particular capacity fade within a battery.